OMNIDIRECTIONAL HYPERSPECTRAL IMAGING

A THESIS SUBMITTED TO
THE GRADUATE SCHOOL OF INFORMATICS OF
THE MIDDLE EAST TECHNICAL UNIVERSITY
BY

NUR DIDEM BAŞKURT

IN PARTIAL FULFILLMENT OF THE REQUIREMENTS FOR THE DEGREE
OF
DOCTOR OF PHILOSOPHY
IN
THE DEPARTMENT OF INFORMATION SYSTEMS

AUGUST 2019

OMNIDIRECTIONAL HYPERSPECTRAL IMAGING

submitted by **NUR DIDEM BAŞKURT** in partial fulfillment of the requirements for the degree of **Doctor of Philosophy in Information Systems Department, Middle East Technical University** by,

Prof. Dr. Deniz Zeyrek Bozşahin
Dean, **Graduate School of Informatics**

Prof. Dr. Yasemin Yardımcı Çetin
Head of Department, **Information Systems**

Prof. Dr. Yasemin Yardımcı Çetin
Supervisor, **Information Systems, METU**

Examining Committee Members:

Assoc. Prof. Dr. Banu Günel Kılıç
Information Systems, METU

Prof. Dr. Yasemin Yardımcı Çetin
Information Systems, METU

Assoc. Prof. Dr. Pekin Erhan Eren
Information Systems, METU

Assoc. Prof. Dr. Yalın Baştanlar
Computer Engineering, IZTECH

Assoc. Prof. Dr. Nazlı İkizler Cinbiş
Computer Engineering, Hacettepe University

Date: 28.08.2019

I hereby declare that all information in this document has been obtained and presented in accordance with academic rules and ethical conduct. I also declare that, as required by these rules and conduct, I have fully cited and referenced all material and results that are not original to this work.

Name, Surname:　Nur Didem Başkurt

Signature　　　:

ABSTRACT

OMNIDIRECTIONAL HYPERSPECTRAL IMAGING

Başkurt, Nur Didem

Ph.D., Department of Information Systems

Supervisor: Prof. Dr. Yasemin Yardımcı Çetin

August 2019, 75 pages

Hyperspectral imaging systems provide dense spectral information on the scene under investigation by collecting data from a high number of contiguous bands of the electromagnetic spectrum. The low spatial resolutions of these sensors frequently give rise to the mixing problem in remote sensing applications. Several unmixing approaches are developed in order to handle the challenging mixing problem on perspective images. On the other hand, omnidirectional imaging systems provide a 360-degree field of view in a single image at the expense of lower spatial resolution. In this thesis, we propose a novel imaging system which integrates hyperspectral cameras with mirrors so on to yield catadioptric omnidirectional imaging systems to benefit from the advantages of both modes. Catadioptric images, incorporating a camera with a reflecting device, introduce radial warping depending on the structure of the mirror used in the system. This warping causes a non-uniformity in the spatial resolution which further complicates the unmixing problem. In this context, a novel spatial-contextual unmixing algorithm specifically for the large field of view of the hyperspectral imaging system is developed. The proposed algorithm is evaluated on various real-world and simulated cases. The experimental results show that the proposed approach outperforms compared methods.

Keywords: Omnidirectional Image Processing, Remote Sensing, Spatial Spectral Unmixing, Omnidirectional Cameras, Catadioptric Cameras

ÖZ

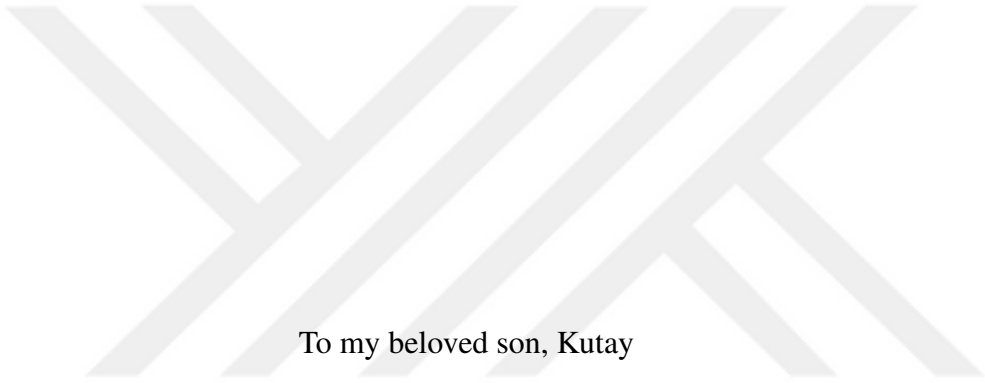## ÇOK YÖNLÜ HİPERSPEKTRAL GÖRÜNTÜLEME

Başkurt, Nur Didem

Doktora, Bilişim Sistemleri Bölümü

Tez Yöneticisi: Prof. Dr. Yasemin Yardımcı Çetin

Ağustos 2019, 75 sayfa

Hiperspektral görüntüleme sistemleri elektromanyetik tayfın ilgili bölgelerinde sık aralıklarla çok sayıda bant üzerinden veri toplayarak görüntülenecek sahne hakkında zengin bir spektral içerik sunar. Uzaktan algılama uygulamalarında, görüntülenecek sahneye göre uzamsal çözünürlüğün yetersiz kalması spektral karışım problemine yol açar. Perspektif görüntülerde bu zor problemi çözmeyi amaçlayan birçok spektral ayrıştırma yöntemi geliştirilmiştir. Diğer yanda, tüm yönlü görüntüleme sistemleri uzamsal çözünürlükten feragat ederek tek görüntüde 360 derecelik görüş alanı sağlarlar. Bu tezde, hiperspektral kameralar ile aynalar beraber kullanılarak yeni bir katadioptrik görüntüleme sistemi tasarlanmış ve her iki kipin de avantajlarından yararlanılmıştır. Katadioptik görüntülerde kullanılan aynanın yapısına bağlı olarak dairesel bir bozulma meydana gelmektedir. Bu bozulma uzamsal çözünürlüğün sahnede eşit dağılmamasına yol açarak hiperspektral görüntülemede karşılaşılan ayrıştırma problemini daha da karmaşık hale getirmektedir. Bu bağlamda, önerilen sisteme özel bir uzamsal spektral ayrıştırma algoritması geliştirilmiştir. Önerilen yöntemlerin başarımları gerçek dünya ve benzetilmiş görüntüler üzerinde değerlendirilmiştir. Deneysel sonuçlar karşılaştırılan yöntemlere göre başarımın arttığını göstermektedir.

Anahtar Kelimeler: Tüm Yönlü Görüntü İşleme, Uzaktan Algılama, Uzamsal Spektral Ayrıştırma, Tüm Yönlü Kameralar, Katadioptrik Kameralar

To my beloved son, Kutay

ACKNOWLEDGMENTS

TABLE OF CONTENTS

ix

LIST OF TABLES

LIST OF FIGURES

LIST OF ABBREVIATIONS

FOV	Field of View
BRDF	Bidirectional Reflectance Distribution Function
PPI	Pixel Purity Index
VCA	Vertex Component Analysis
SPP	Spatial Preprocessing
RBSPP	Region Based Spatial Preprocessing
SSPP	Spatial-Spectral Preprocessing
AMEE	Automated Morphological Endmember Extraction
NNLS	Non-negativity Constrained Least Squares
EEA	Endmember Estimation Algorithm
HySime	Hyperspectral Signal Identification by Minimum Error
AME	Abundance Map Extraction
NIR	Near Infrared
VNIR	Visible-Near Infrared
FTIR	Fourier Transform Infrared

CHAPTER 1

INTRODUCTION

Hyperspectral imagery provides dense spectral information about the material, it attracts interest of researchers working in the fields of computer vision and remote sensing. Remote sensing applications aim to monitor large observation fields in a rapid way with a nondestructive manner. The existing studies on remote sensing and hyperspectral imaging applications utilize the platforms which are mostly mounted on airborne or unmanned air vehicles (UAV) in order to monitor large areas. However, airborne platforms have operational difficulties such as inappropriate weather conditions, flight permissions, no fly zones, and costly aircraft hire. In addition, UAVs have limitations on the load of the imaging system containing heavy imaging hardware such as sensor and processing unit. Although, recently hyperspectral camera producers focus on decreasing weight of the systems, this is still a high concern. In the study, we aim to increase the field of view (FOV) of traditional hyperspectral imaging systems which use lenses having narrow FOV. Therefore, we contribute to existing hyperspectral and multispectral imaging systems with providing a large field of view. Fish-eye lenses, stitching several images captured by a narrow FOV camera, and catadioptric systems are examples for large FOV imaging systems. Catadioptric cameras are the optical systems in which refraction (lenses) and reflection (mirrors) are combined. While these systems produce a deformation in the structure of the image due to the convex mirror used in the system, they are able to present 360 degree FOV in the horizontal plane. The term omnidirectional is used to denote that the light rays from all directions are collected.

In the study, we aim to benefit from hyperspectral imaging and omnidirectional imaging technologies to obtain a catadioptric omnidirectional hyperspectral camera, and to handle the issues arising due to combining these technologies. There are very few reported studies which use high spectral information for omnidirectional imaging. These studies are summarized in Section 1.2. The low spatial resolution of the sensors frequently bring about the mixing problem in hyperspectral imaging applications. Several unmixing approaches are developed in order to handle the challenging mixing problem on perspective images. To our knowledge ours is the first study that investigates the applicability of unmixing algorithms for omnidirectional hyperspectral images. We propose capturing a single omnidirectional image without requiring a prior stitching step.

The performance of the image processing algorithms, the robustness of the results and the detailed information provided by the sensors are highly dependent on the in-

1

creased spectral and spatial resolution of the data. The conventional hyperspectral imagers renounce the high spatial resolution in favor of the high spectral resolution. Today's remote sensing technology on satellite and airborne applications is limited with the constraints: data storage capacity, the transmittance broadband between the imager and ground station, the weight limit to be carried on [7]. These constraints cause to have a lower spatial resolution which obstructs to measure the spectral signature of the object to be analyzed. In this case, the pixels captured in such scenario may not purely contain a single material. The pixel is mixed of the spectral signatures of the objects which are in the scene that are spatially covered by the pixel. At that point, a sub-pixel level analysis is needed, and this wide research area is termed as spectral unmixing. Additionally, the pure spectra of the materials which exist in the scene, are called as endmembers.

Research Objectives and Significance of the Study

- Using line scan cameras on catadioptric systems

- Developing unmixing and potentially other algorithms specialized for these imaging system

The Contributions of the Study

The catadioptric hyperspectral image analysis requires different unmixing approaches compared to the traditional hyperspectral image analysis. In this study, some improvements specific to the catadioptric images on unmixing algorithms are proposed. Although we present a case which uses a catadioptric imaging system, the omnidirectional hyperspectral imaging system can contain a fish-eye lens where the mentioned unmixing problem for such systems is also valid.

All the proposed methods are based on the spatial resolution factor of the pixels. Therefore, the literature on catadioptric image formation is analyzed in depth. These studies enable us to compute the spatial resolution factor of each pixel in the scene, and consequently to generate a map that illustrates the change on the spatial resolution values.

The first proposed improvement is for integrating the spatial resolution difference into the geometrical and spatial-contextual unmixing methods. We also theoretically examined the contribution of implementing the spatial resolution map into unmixing algorithms.

The spatial-spectral unmixing approaches integrate the spatial information with the spectral unmixing approaches where this integration can be done as a preprocessing step of the spectral analysis or it can be performed concurrently. Traditional unmixing approaches assume the spatial equality of the area covered by each pixel. In other words, the distance between two pixels is evaluated equal on every part of the image. However, a new concern occurs for catadioptric unmixing approach. The spatial analysis of spectral unmixing algorithms need to consider the catadioptric mirror structure. We propose such an improvement for spatial-spectral unmixing algorithms.

2

Another improvement is proposed for geometrical unmixing approaches. Most of the geometrical approaches in the literature assume that the hyperspectral data is spread in a convex structure. As explained in the previous proposed method, each pixel in catadioptric image has different spatial resolution factor. Therefore, the mixing ratio of the pixels depend on their spatial resolution. The pixel with a higher spatial resolution is more likely to contain a pure signature, in other words less mixed signature. We propose to rate the pixels in the convex structure according to their spatial resolution factors.

The last novel improvement is proposed for local spectral mixing analysis approach. The local unmixing algorithms spatially divide the hyperspectral scene rather than inspecting the whole scene at once. This point of view in unmixing problem produces more robust and accurate results. We give justifications based on the literature studies.

The Road Map

This study is organized as follows:

Introduction chapter continues with the basic concepts, advantages, constraints, and application areas of both technologies: hyperspectral imaging and omnidirectional imaging. Chapter 2 begins the study with a simple introduction to catadioptric imaging principles. We also investigate the spectral characteristic of the mirror used in the omnidirectional imaging.

The main research area of the study is the unmixing problem in hyperspectral imaging applications. Chapter 3 provides information about unmixing problem, and state-of-the-art algorithms. We aim to make this problem clear for the readers who are more familiar with omnidirectional imaging. We also present brief experimental results for the sub-processes of the unmixing approach.

Chapter 4 presents the novel approaches which are specially investigated for the proposed catadioptric hyperspectral imaging system. The evaluation of the proposed methods are given in Chapter 5. The comparison of the methods with the state-of-the-art algorithms are also shared in the chapter. Finally, a conclusion part is given in the end of the dissertation.

1.1 Hyperspectral Imaging

A three-dimensional hyperspectral data cube is obtained by measuring the spectral signature of each pixel. While the first two-dimensions represent the spatial domain of the scene, the third-dimension represents the data gathered from each spectral band.

The data measured by hyperspectral sensor is the so called digital number (DN) which is not meaningful before calibration using sensor parameters and the illumination in the scene. To put it more explicitly, different DN values of an object can be measured in different acquisition conditions as using different camera and illumination conditions. After applying gain and offset values of the hyperspectral sensor, data

is converted to radiance which is the amount of radiation coming from the scene. Yet radiance still is not able to represent the spectral features of the material. For quantitative analysis of hyperspectral data, radiance unit is corrected to reflectance unit. The radiation reflected from the surface is affected from the illumination of the scene. The sun is naturally the source of illumination for outdoor acquisitions. The solar spectrum peaks at approximately 500 nm, and shows low radiation at irregular intervals after NIR region of electromagnetic spectrum. The atmospheric correction algorithms must be used in order to compensate the solar spectrum effect.

Although hyperspectral sensors make significant contribution to spectral analysis applications by frequent measurements on electromagnetic spectrum, they may also have a disadvantage in processing of data due to their high dimensionality. Therefore dimensionality reduction and band selection algorithms are often implemented to increase the performance of the algorithm and discard redundant information. Latorre-Carmona et al. [8] observe the effect of denoising in band selection by comparing several algorithms. Bruce et al. [9] use discrete wavelet transform, and J. Wang & Chang [10] use independent component analysis in order to reduce dimensionality of hyperspectral image.

Hyperspectral imagery is preferred in a wide array of remote sensing applications. Improvements in sensor technologies enable to lower costs and weight, and make the use of sensor more practical. Hyperspectral imagery is increasingly employed in agriculture. Plants have distinguishable spectral characteristics on different regions of electromagnetic spectrum. Furthermore they demonstrate different spectral characteristics in their each growth phase. Therefore studies in the literature show that spectral analysis in agriculture applications is highly useful to classify the plants and detect their growth period. Jia et al. [11] aim to analyze spectral discrimination of four closely planted species: wheat, poppy, barley, and alfalfa. Hyperspectral analysis algorithms used in agriculture applications commonly benefit from spectral mixture analysis methods due to the low spatial resolution of hyperspectral data. The area covers a pixel of hyperspectral image is mostly greater than the canopy area of the tree or the size of the target leaf. Therefore the pixel is expected to be mixed by spectra of more than one object. The studies in the literature utilize unmixing and spectral mixture analysis algorithms as given in [12], [13].

1.2 Omnidirectional Imaging

Omnidirectional cameras are composed of catadioptric systems where refraction and reflection are combined in an optical system: curved mirrors (catoptric) and lenses (dioptric). In recent years, omnidirectional imaging systems are preferable with a 360 degree field of view (FOV) in the horizontal plane in image processing applications. This enlarged view property enables to capture the scene by using a single camera instead of many perspective cameras.

As catadioptric systems can be composed of many planar mirrors [14], they can also benefit from single curved mirrors, where paraboloidal and hyperboloidal mirrors are

4

the most popular ones. However, in this study we focus on catadioptric systems with a single mirror. Bastanlar [15] briefly explains single-viewpoint property of catadioptric systems. The light rays coming from the scene and targeting the focal point (single viewpoint) of the hyperboloidal mirror are reflected on the mirror surface so that they pass through the pinhole (camera center). On the other hand, paraboloidal mirrors reflect the rays orthogonally and that's why they require the use of a telecentric lens to collect the parallel rays.

The application areas such as surveillance and simultaneous localization and mapping (SLAM) highly need a system that is easy to use, and captures wide field of view in a single image. Thus, it enables fast analysis of the scene without need of the installment of several cameras with different angles. Aeromeccanica [16] presents an unmanned aerial vehicle equipped with an omnidirectional camera with two optics having more than 200 degree FOV. Additionally, an infrared (IR) camera is also mounted on the drone.

Technest, is transferred to under the umbrella of Genex Technology Solutions, has been awarded by U.S. Navy Small Business Innovative Research program with the project [17] "Real-Time Omni-Directional Hyperspectral Imager". The system called Omni-Guard proposes to develop a real-time omnidirectional hyperspectral recording and processing imager. It uses compact mega pixel infrared and mid-wave infrared capable sensors and supposed to capture a 360 degree field of view by using a rotating system that captures 180 degree FOV at a time. Similarly, a rotating spectral imaging system is used in order to capture large field of view in the studies [18], [19], [20]. Hirai et al. [18] combine three technologies: HDR, spectral and omnidirectional imaging. They use an automatically rotating mechanism. An RGB camera is supported by filters in order to acquire 6 band multispectral data between 400 nm and 700 nm. They perform a correction algorithm on spectral images to reduce the illumination related noises. Karaca et al. [19] develop a multiband stereo matching algorithm on a panoramic stereo hyperspectral imaging system. Additionally, they perform a depth estimation on panoramic hyperspectral dataset. However, in this study, we propose to develop an omnidirectional hyperspectral system that captures 360 degree FOV in a single image without using a rotating mechanism.

Danilidis et al. [21] has filed a patent with the title "Multispectral Omnidirectional Optical Sensor and Methods Therefor". It provides a multispectral and omnidirectional imaging system that contains a series of view and reflecting mirrors for splitting the electromagnetic spectrum into two or more bands, and corresponding cameras placed relative to the reflecting mirrors. Although the system is innovative for its time, its multispectral representation capacity is well behind today's technology.

In terms of hyperspectral omnidirectional imaging, there are few previous studies. The closest work to ours, presented in [22], records a plenoptic function of the scene from every location, at every angle, for every wavelength and at every time. They use 3×3 spectral coated catadioptric mirrors. They perform a sparse representation on depth estimation problem by using the system. However, the spectral density of their proposed system depends on the number of mirrors. Our work, on the other hand, is

entirely hyperspectral and we investigate unmixing approaches in catadioptric domain for the first time.

Omnidirectional images inevitably introduce a radial warping due to the structure of the mirror used in the system. As some of the studies [23], [24], [25], [26] develop algorithms without modifying the elliptic structure of the scene, others [27], [28], [29], [30] prefer to transform the image to the panoramic view, and work on linear representation. For the applications where the spatial nonuniformity does not affect the performance of the algorithm, we aim to avoid the costly process of generating panoramic view. Thus, we benefit the spectral content of the pixel without need of spatial linearity. Hyperspectral imaging with its high spectral density adds value to remote sensing applications due to its spectral density rather than its provided spatial information.

CHAPTER 2

HYPERBOLOIDAL CATADIOPTRIC SYSTEM

In this chapter, the hyperboloidal catadioptric system is investigated. A preliminary research objective of this dissertation is to analyze the spectral effect of the mirror used in the proposed system. In the first subsection, image irradiance is studied. In the second part, related work on mirror material and its reflectance signature are presented. Additionally, some measurements on omnidirectional hyperspectral system are shown to investigate the mirror effect. Lastly, hyperboloidal image formation is studied.

The proposed omnidirectional hyperspectral imaging system is illustrated in Figure 1. The system is composed of a hyperspectral camera and a hyperboloidal mirror. The scheme demonstrates a representation of an omnidirectional hyperspectral data cube. It also shows the spectral signature gathered from a pixel in the data cube. A sample omni-hyperspectral image acquisition setup is shown in the figure. Finally, an unwrapped visualization of the omnidirectional image is given in the scheme.

2.1   Image Irradiance

Bidirectional reflectance distribution function (BRDF) defines the ratio of the radiance in the outgoing direction to the incident irradiance. The function is formalized as [1]:

$$f_r(\theta_i, \varphi_i, \theta_r, \varphi_r) = \frac{\mathrm{d}L_r(\theta_r, \varphi_r)}{\mathrm{d}E_i(\theta_i, \varphi_i)} = \frac{\mathrm{d}L_r(\theta_r, \varphi_r)}{L_i(\theta_i, \varphi_i)\cos\theta_i\mathrm{d}\omega_i} \tag{1}$$

where f_r is the BRDF function, the reflected radiance in the direction (θ_r, φ_r) is $\mathrm{d}L_r$, and $\mathrm{d}E_i$ is the incident irradiance with the angle θ_i and $\mathrm{d}\omega_i$ is the solid angle element within which the incident radiance is confined. The geometry of incident and reflected elementary beams are illustrated in Figure 2a.

Traditionally, optical propagation has been treated as consisting of two distinct phenomena: regular (specular) propagation and diffuse propagation. However, while purely regular (specular) or purely diffuse propagation can be very closely approximated, neither is ever completely and independently achieved in practice. Reflection difference of these phenomena is demonstrated in Figure 2b and c.
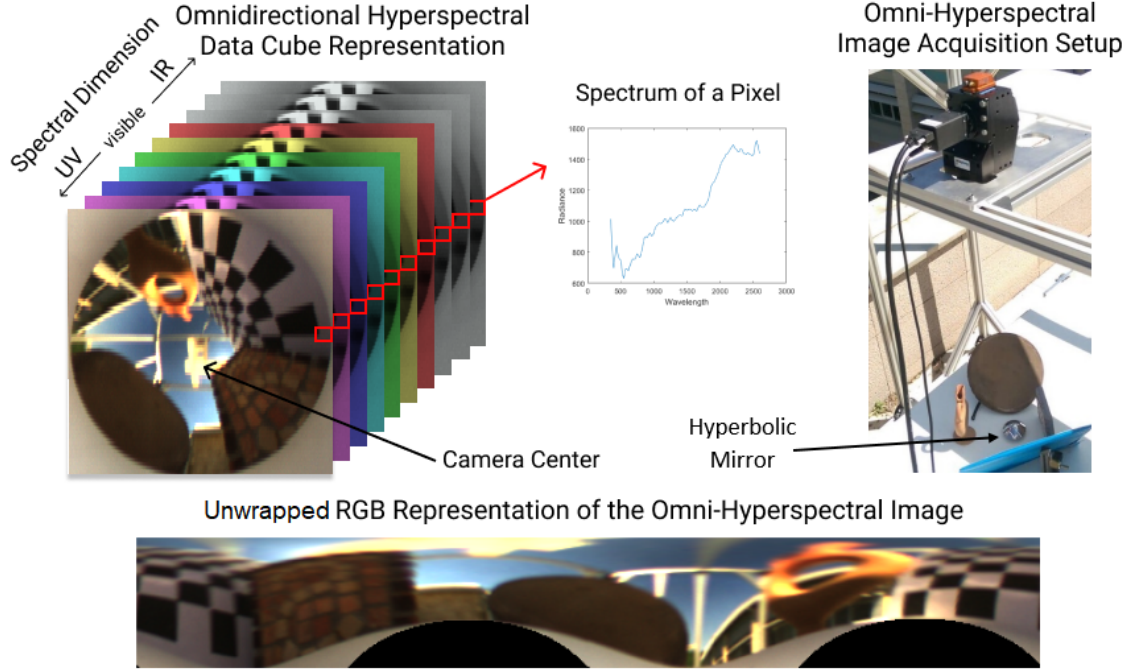
Figure 1: The proposed omnidirectional hyperspectral imaging system consists of a convex (hyperboloidal) mirror and a hyperspectral camera looking at the mirror.

There are several BRDF models that aim to model the surface reflection. The Lambertian Surface appears equally bright from all viewing directions and reflects all incident light. The Lambertian surface is an ideal diffuser as it is independent from the viewing direction. The BRDF of Lambertian surface is:

$$I = \frac{\rho}{\pi} k c \cos \theta_i \tag{2}$$

where k is source brightness, ρ is surface albedo (reflectance), c is constant (optical system), θ_i is the angle of incident light, and I is image irradiance.

The reflection of a world point to the mirror surface is illustrated in Figure 3. In the example shown in Figure 3, the incoming light from the sun is reflected to the object with an angle θ_i and then to the mirror surface. The outgoing radiance is effected by the angle of the light and the surface reflectance. In the proposed system, the radiance is effected by both diffuse and specular propagation. While the reflection from the object represents the diffuse propagation, mirror reflection is the specular propagation. We propose to approximately formulate the radiance obtained in the camera as

$$I = \left(\frac{\rho_{body}}{\pi} k c \cos \theta_i \right) \rho_{mirror} \tag{3}$$

.

Figure 3 illustrates the scene to be captured in the proposed system. Bastanlar indicated in his study [31] that catadioptric systems are able to provide single-viewpoint property if the mirror has a focal point which can behave like an effective pinhole. In
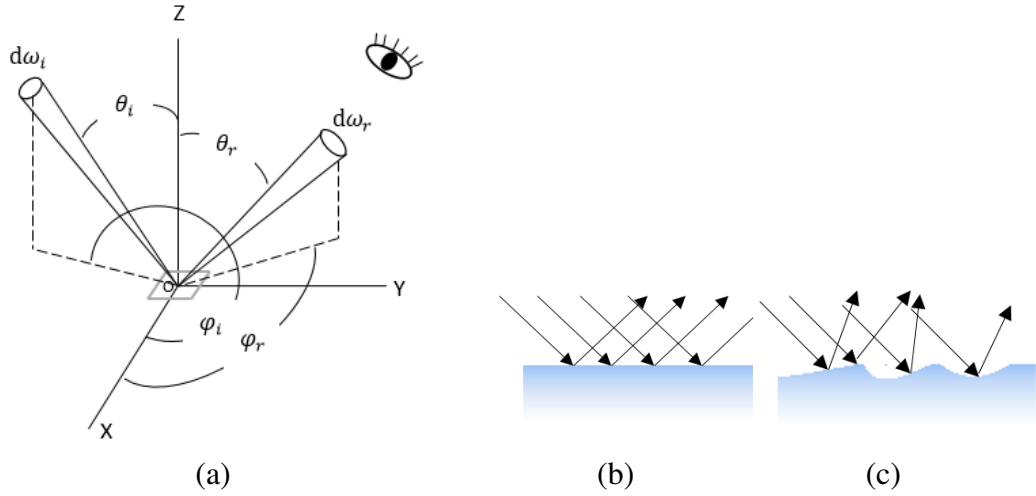
Figure 2: (a) Geometry of incident and reflected elementary beams [1]. (b) Specular reflection. (c) Diffuse reflection.

Figure 3, the light ray coming from the world point and targeting the focal point of the hyperboloidal mirror is reflected on the mirror surface. The reflected ray passes through the camera center (effective pinhole).

2.2 Stainless Steel Mirror Spectral Characteristics

As discussed in Section 2.1, the intensity value measured in the hyperspectral sensor is dependent on the source brightness, angle of the irradiance vector, diffuse reflectance of the object and the specular reflectance of the mirror. Therefore the material of the mirror plays a critical role in the measured intensity value. In this section, literature study on the material of the mirror is presented. In the experimental studies, we used Neovision Hyperbolic Stainless Steel Mirror.

Benlattar et al. [2] indicate that stainless steel with high visible band reflectance and high infrared band emissivity can be used as a good radiative cooling material. They performed their experimental studies on borosilicate glass substrate coated with stainless steel thin film. The effect of film thicknesses on the reflectance signature is shown in Figure 4a.

Another study on stainless steel reflectance which is presented by Rooms et al. [3], is about using metal foils in order to optimize the efficacy and angle dependence of emission of top-emissive organic light-emitting diodes. The PEDOT used under the metal foils causes a dip at 480 nm as shown in Figure 4b.

In the study of Marot et al. [4], they aim to optimize the performance of the first mirror used in ITER plasma diagnostic systems. The first mirror is deemed as one of the most critical elements of these systems. Because it must survive in an extreme environment
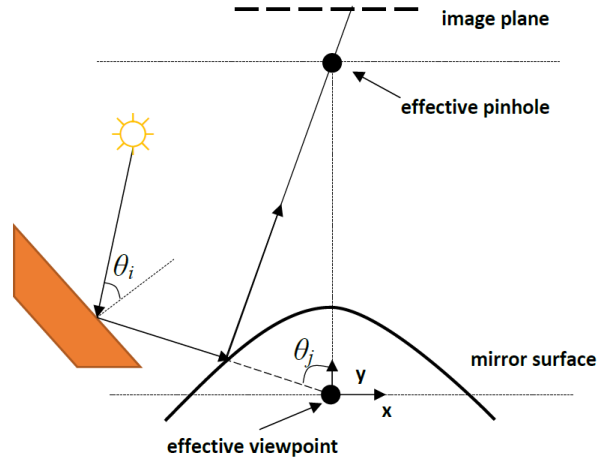
Figure 3: Image formation of hyperboloidal catadioptric systems.

| (a) | (b) | (c) | (d) |
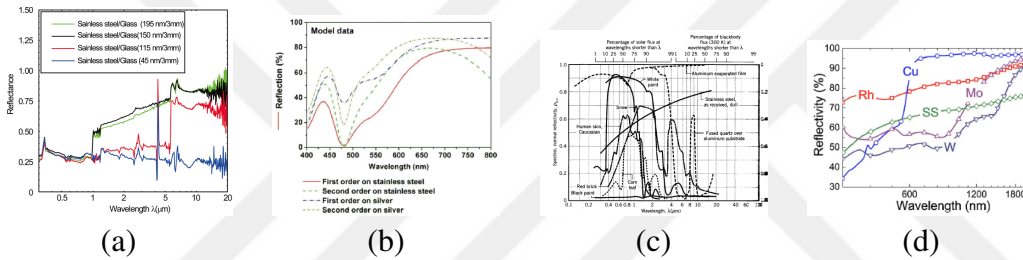
Figure 4: (a) Stainless steel reflectance characteristics. [2], [3], [4], [5]

such as intense UV and x-ray radiations, Rhodium is an attractive material for this purpose thanks to its high reflectivity in the visible wavelength range and its low sputtering yield. However, the very high price of rhodium calls for its use in the form of a film deposited onto metallic substrates. Stainless steel is analyzed as an alternative substrate. The reflectance signature of the stainless steel between 300 nm – 1800 nm is presented in Figure 4c (SS).

In the literature, it is seen that stainless steel is frequently preferred thanks to its high reflectivity and low price comparing to other metals. Finally, Figure 4d [5] demonstrates several materials' reflectance measurements including stainless steel.

Some Experiments on Spectral Effect of the Mirror

In this experiment, several materials with a diverse signature are captured in order to observe the effect of mirror on reflected signature.

The scene to be analyzed is shown in Figure 5. Firstly, four points are selected from the objects, and then their corresponding points on the mirror. Median signatures of the four points selected on each object are plotted in Figure 5c. An initial analysis on the spectra shows that the mirror reduces the intensity values of the objects' original

10

spectra. This is expected because some of the incident light may be absorbed by the mirror and the remainder will be reflected.

The effect of the mirror is gathered from the Eq. 3 given in Section 2.1:

$$\rho_{mirror} = \frac{I}{\frac{\rho_{body}}{\pi} kc \cos \theta_i}$$ (4)

where I is the radiance measured on the sensor, ρ_{mirror} and ρ_{body} are the mirror and object reflectance respectively, k is source brightness, c is constant about the optical system, and θ_i is the angle of the irradiance. The computed mirror reflectance signature is shown in Figure 5d. This analysis provides to deduce that spectral effect of the mirror is quite linear which is probably caused by the decline in the source of illumination. In conclusion, the spectral effect of the mirror is negligible on hyperspectral data processing algorithms.

2.3   Catadioptric Image Formation

In the proposed system the spatial resolution decreases from periphery of the omnidirectional image to its center. In this study, we have demonstrated this effect both theoretically and practically. Baker and Nayar presented the single-viewpoint geometry of the catadioptric image formation in their fundamental work [32]. They deeply analyze the different mirror shapes which are used in the catadioptric system. An expression for the spatial resolution factor of a catadioptric sensor is derived in the study. They also include a preliminary analysis of the defocus blur caused by the use of a curved mirror. Baker and Nayar demonstrate in detail the spatial resolution change due to the image coordinate. However, they set a precondition on this computation: the camera must be localized in the effective pinhole of the catadioptric system.

Baker and Nayar [32] present a factor that computes the spatial resolution of the image acquired by the catadioptric mirror. The factor is based on a condition which assumes that while the mirror is positioned in the effective viewpoint v, the camera must be positioned in the effective pinhole p. In Figure 6, the mirror geometry is illustrated in detail based on the studies in [32], [33]. The mirror parameters are a, b and c where c is the distance between pinhole and viewpoint in other terms the camera and the mirror, and c is given by $c = 2\sqrt{a^2 + b^2}$.

The variables used in the following equations are demonstrated in Figure 6. As described in [32], the resolution of the catadioptric sensor is dA/dv where dA is the pixel area on the image and dv is the infinitesimal solid angle viewing the world. The resolution of the conventional camera was derived in [32] as:

$$\frac{dA}{d\omega} = \frac{u^2}{\cos^3 \psi}$$ (5)

11

(a)   (b)

(c)

(d)
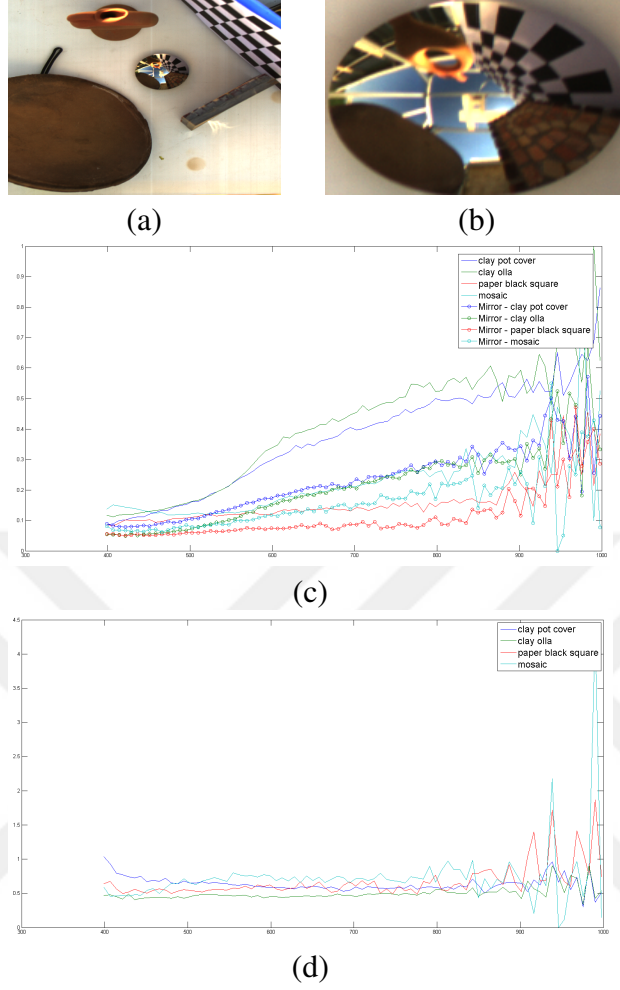
Figure 5: (a) RGB representation of the experiment scene. (b) Mirror area. (c) Spectral signatures of materials. (d) Spectral effect of stainless steel mirror

Then, the area of the mirror $(\mathrm{d}S)$ imaged by the infinitesimal area $(\mathrm{d}A)$ is:

$$\mathrm{d}S = \frac{\mathrm{d}\omega \cdot (c-z)^2}{\cos\phi\cos^2\psi} = \frac{\mathrm{d}A \cdot (c-z)^2 \cdot \cos\psi}{u^2 \cos\phi} \tag{6}$$

The solid angle $\mathrm{d}v$ can be defined as:

$$\mathrm{d}v = \frac{\mathrm{d}S \cdot \cos\phi}{r^2 + z^2} = \frac{\mathrm{d}A \cdot (c-z)^2 \cdot \cos\psi}{u^2(r^2 + z^2)} \tag{7}$$

where (r, z) is the point on the mirror being imaged. Hence the equation of resolution of catadioptric sensor can be re-written as:

$$\frac{\mathrm{d}A}{\mathrm{d}v} = \frac{u^2(r^2 + z^2)}{(c-z)^2 \cdot \cos\psi} = \left[\frac{(r^2 + z^2)\cos^2\psi}{(c-z)^2}\right]\frac{\mathrm{d}A}{\mathrm{d}\omega} \tag{8}$$

12

But, since:

$$\cos^2 \psi = \frac{(c-z)^2}{(c-z)^2 + r^2} \tag{9}$$

we have:

$$\frac{\mathrm{d}A}{\mathrm{d}v} = \left[\frac{r^2 + z^2}{(c-z)^2 + r^2}\right]\frac{\mathrm{d}A}{\mathrm{d}\omega} \tag{10}$$

The resolution of the catadioptric camera is the multiplication of the resolution of the conventional camera with the factor res which is given by:

$$res = \frac{r^2 + z^2}{(c-z)^2 + r^2} \tag{11}$$

Note that the factor in (11) is the square of the distance from the point (r, z) to the effective viewpoint v divided by the square of the distance from the point (r, z) to the pinhole p. Hence the spatial resolution is highest around the periphery.
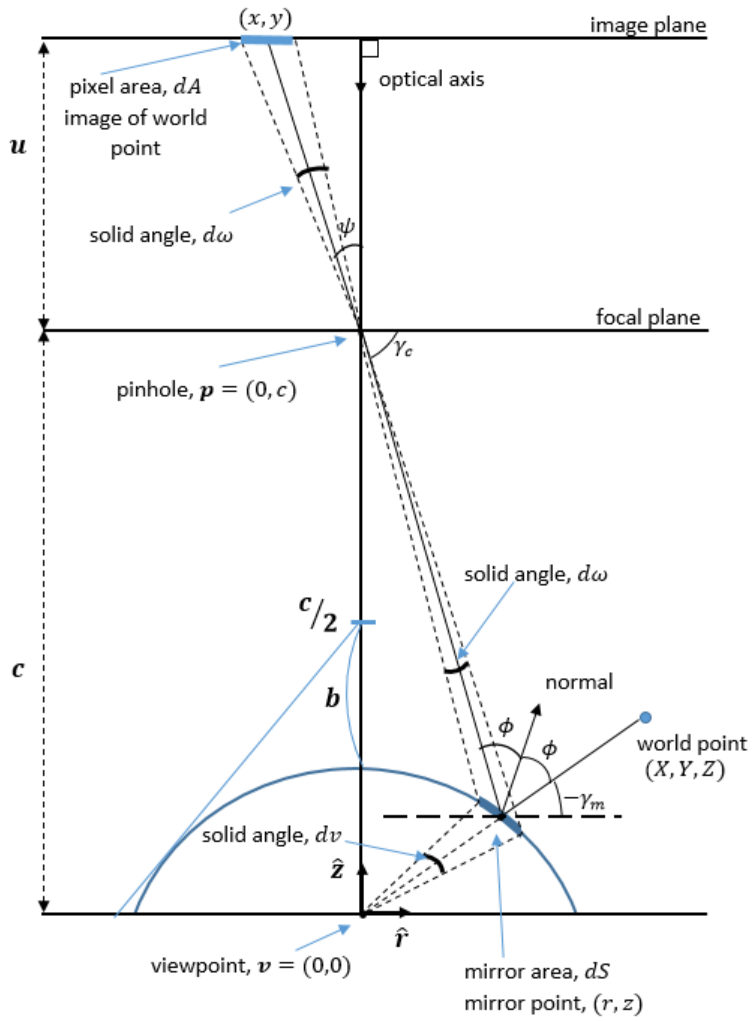
Figure 6: Image formation in a catadioptric camera with a hyperboloidal mirror.

CHAPTER 3

HYPERSPECTRAL UNMIXING

The chemical information stored in the hyperspectral data cube provides higher performance on classification, identification and target detection problems in image processing applications compared to the conventional imaging systems [34]. Traditional image processing applications assume that a pixel corresponds to the reflectance value of a single material. However, especially in remote sensing applications, the neighboring objects can be captured in a single pixel. Hyperspectral imaging makes it possible to discriminate and identify the different materials existing in a pixel, and their corresponding mixing ratios. The pure spectral signature of a material is called as an endmember. The unmixing approach is an umbrella term that encompasses three main steps: estimation of the number of endmembers, estimation of endmember spectra and estimation of their abundances. The abundance of endmember determines the proportion of the endmember in a pixel. The general definition of a mixed data is:

$$x_{ij} = \sum_k e_{ik} c_{kj} + n_{ij} \tag{12}$$

where x_{ij} is the intensity of the ith band of the jth pixel, e_{ik} is the spectrum of the ith band of the kth endmember, c_{kj} is the mixing proportion for the jth pixel from the kth endmember, and $\mathbf{n}$ is random noise. Assuming the ideal case where noise is zero, and j^{th} pixel purely contains a single material. The $\mathbf{c}_k$ becomes 1, and the $L \times 1$ vector $\mathbf{x}_j$ is equal to $\mathbf{e}_k$ where L is the number of bands. The mixing proportions should sum to one, i.e:

$$\sum_k c_{kj} = 1 \tag{13}$$

Figure 7 illustrates a basic mixing scenario. Assume that this is a remotely captured hyperspectral image of a vegetation field. Each color represents different plant species. The pixel borders are illustrated by black colored grids. The coordinate system is given in (x, y) format, where $x = 1, \ldots, 6$ and $y = 1, \ldots, 6$. If we examine the scenario according to the expressions given in Eq. 12 and 13, where $k = 1, \ldots, 8$. For example, the pixels in coordinates $(1, 1)$, $(2, 1)$, $(1, 6)$, and $(6, 1)$ are pure pixels of endmembers 1, 1, 3 and 7, respectively. The pixel which highlighted with white borders $(j = 10)$ is an example for a mixing case of endmembers 2 and 5. Figure 7b plots the spectra of pure endmember 2 and endmember 5 (The colors in Figure 7a and b are corresponding to each other). The noise is ignored in this example. The mixing ratios
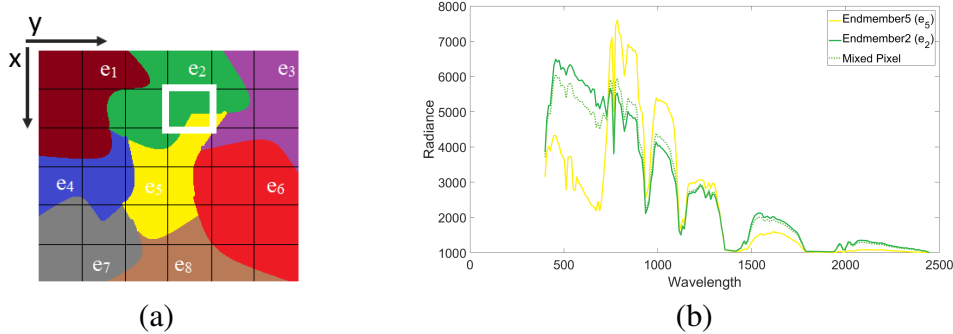
Figure 7: A basic illustration for the mixing scenario.

are 80 percent of $\mathbf{e}_2$ and 20 percent of $\mathbf{e}_5$. The mixing is as follows:

$$\mathbf{x}_{10} = (\mathbf{e}_2 \times 0.8) + (\mathbf{e}_5 \times 0.2) \tag{14}$$

The spectral signature of the mixed pixel is also plotted in Figure 7b with light green dotted line. The spectra used in this example are gathered from Indian Pines [35] dataset: e_2 is the median spectral signature of the 16th class, and e_5 is the median of 14th class.

The scattered energy is measured as a mixing of the endmember spectra by the sensor. When the mixing scale is macroscopic, the linear mixing models are used [36]. However, for the microscopic mixing scale, the linear model is no longer accurate, and nonlinear models are required [37]. In this study, linear unmixing models are considered. In linear mixing problems, the mixing occurs within the sensor due to the low resolution in contrast to the nonlinear mixing case. In this case, all objects in the scene are exposed to the same irradiance. However, the linear mixing is encountered in the pixels which contain more than one material. The low spatial resolution prevents the measurement of their reflectance signatures individually. Although the linear mixing model is technically simple and clear, it remains incapable in such scenarios where a physical interaction occurs due to the scattered light from several surfaces. In such a scenario, the mixing is nonlinear. Additionally, the nonlinear mixing can be observed in homogeneously mixed materials. On the other hand, albedo effect is another type of nonlinear model where reflectance is a nonlinear function of albedo [38]. Most of the studies in the literature including the proposed algorithm in this study are devoted to the linear mixing model. The reason is that, despite its simplicity, it is an acceptable approximation of the light scattering mechanisms in many real scenarios.

Bioucas-Dias et al. [38] present a comprehensive overview on hyperspectral unmixing. They first discussed the linear and nonlinear mixing models, and then briefly summarized the preprocessing steps of unmixing. They divide mixing models into five categories as signal subspace, geometrical, statistical, sparsity-based, and spatial-contextual algorithms. In recent years however, deep learning has attracted much attention in many domains. Zhang et al. [39] used a convolutional neural network

16

architecture that first extract spectral-spatial features and then obtain abundance percentages. They present their work using both pixel-based and cube-based architecture.

In Section 3.1, the method used in this study to compute the input parameter required by the unmixing models is discussed in detail. In Section 3.2 and Section 3.3, geometrical and spatial-contextual categories of the mixing models are studied, the prominent algorithms in these categories explained and compared theoretically. The geometrical approaches are analyzed on their pseudocodes. The flowcharts of the spatial-spectral approaches are presented in the corresponding section. In Section 3.4, the abundance estimation method used in this study is briefly discussed, and the abundance approach is visually explained on a sample acquisition.

3.1 Estimation of Number of Endmembers

Most of the unmixing approaches in the literature assume that the hyperspectral data is spread in a convex structure, and this assumption is used as a base for endmember extraction. However, this assumption requires the number of the pure materials to be known apriori. Hyperspectral Signal Identification by Minimum Error (HySime) developed in the study [40] is one of the well-known algorithms in the literature for estimating the number of endmembers. We implemented HySime for this purpose in our proposed algorithm. The method is an unsupervised eigen-decomposition based approach. It first estimates the signal and noise correlation matrices and then selects the subset of eigenvalues of signal correlation matrix that best represents the signal subspace in the least squared error sense. Best representation is defined as the subspaces where the difference between signal and noise (Eq. 15) is higher than zero. The number of eigenvalues where the difference is positive, are determined as the number of endmembers (k).

$$(\hat{k}, \hat{\pi}) = \arg\min_{k,\pi} \left\{ c + \sum_{j=1}^{k} -\mathbf{p}_{ij} + 2\boldsymbol{\sigma}_{ij}^2 \right\} \tag{15}$$

where c is an irrelevant constant, and $\hat{\pi}$ determines the best permutation. $i = 1, \ldots, L$ where L is number of bands. $\mathbf{p}_{ij}$ and $\boldsymbol{\sigma}_{ij}^2$ are quadratic forms given by

$$\mathbf{p}_{ij} = \mathbf{e}_{ij}^T \hat{\mathbf{R}}_y \mathbf{e}_{ij} \tag{16}$$

$$\boldsymbol{\sigma}_{ij}^2 = \mathbf{e}_{ij}^T \hat{\mathbf{R}}_n \mathbf{e}_{ij} \tag{17}$$

$\hat{\mathbf{R}}_y$ is the sample correlation matrix, $\hat{\mathbf{R}}_n$ is the estimated noise correlation matrix, and $\mathbf{e}_i, \ldots, \mathbf{e}_L$ are the eigenvectors of signal correlation matrix.

The reader is kindly directed to the study presented in [40] for the detailed explanation of relation between the noise and sample correlation matrices and the corresponding minimization purpose of the algorithm.

3.2 Geometrical Unmixing Approaches

In the literature, geometrical studies are mostly preferred due to their high performance and low computational complexity. The geometrical-based approaches are categorized into two main categories: pure pixel based and minimum volume based [38]. Well known algorithms Pixel Purity Index (PPI) [41], N-FINDR [42], and Vertex Component Analysis (VCA) [43] assume the existence of pure pixels for each endmember. The other category that covers the minimum volume based algorithms, seeks a mixing matrix that minimizes the volume of the simplex containing the data. The following subsections explain the details of PPI, N-FINDR and VCA algorithms briefly.

3.2.1 Pixel Purity Index (PPI)

The pixel purity index (PPI) [41] algorithm projects every spectral vector onto skewers, defined as a large set of random vectors. The points corresponding to extrema, for each skewer direction, are stored. A cumulative account records the number of times each pixel is found to be an extreme. The pixels with the highest scores are the purest ones. The algorithm iterates as the number of skewers (num_skewers). PPI requires lower computational cost than N-FINDR according to the number of iterations. Although, PPI is one of the early developed methods, it still takes place in researches. The pseudo code of the algorithm is provided in Algorithm 1.

Algorithm 1 Pixel Purity Index (PPI) Algorithm

Input p, $\mathbf{R} \equiv [r_1, r_2, \ldots, r_N]$, *num_skewers* {*num_skewers* is the number of skewer vectors to project data onto.}

Output M {$\mathbf{M}$ is a $L \times p$ estimated mixing matrix}

1: **skewers** := randn(L,*num_skewers*);{normally distributed $L \times num\_skewers$ samples}
2: **votes** := zeros(N,1);
3: **for** $i := 1$ to *num_skewers* **do**
4: vol_aux := **skewers**$_{:,i}\mathbf{R}_0$; {$\mathbf{R}_0$ is the zero-mean of $\mathbf{R}$}
5: vol_aux := abs(vol_aux);
6: [max_vol,idx] := max(vol_aux); { idx is the indice of the data extreme }
7: [**votes**]$_{idx}$:= [**votes**]$_{idx}$ + 1;
8: **end for**
9: [val_aux,indice] := sort(**votes**); { sortes votes in descending order}
10: indice := [indice]$_1$: p;
11: $\mathbf{M}$:= $[\mathbf{R}_0]_{:,indice}$;

3.2.2 N-FINDR: An Algorithm For Fast Autonomous Spectral End-member Determination In Hyperspectral Data

N-FINDR [42] is based on the fact that in spectral dimension the volume defined by a simplex formed by the purest pixels is larger than any other volume defined by any other combination of pixels. Therefore, all pixels are evaluated in the algorithm. This algorithm finds the set of pixels defining the largest volume by inflating a simplex inside the data. The number of iterations is equal to number of pixels times number of endmembers $(N \times p)$.

The algorithm tries to find the pure pixels by searching each pixel in the data. The technique is based on the fact that in N spectral dimensions, the N-volume contained by a simplex formed of the purest pixels is larger than any other volume formed from any other combination of pixels [42]. For each combination of endmember set, the volume is recalculated. The volume (v) of the simplex formed by using the endmember estimation is proportional to the determinant of endmember matrix (E):

$$V(E) = \frac{1}{(l-1)!} abs(|E|) \tag{18}$$

where $(l-1)$ is the number of dimensions occupied by the data. The pseudo code of the algorithm is provided in Algorithm 2. The number of iteration is quite larger than PPI and VCA. However, it significantly produces more accurate results than PPI.

Algorithm 2 N-FINDR

Input p, $\mathbf{R} \equiv [r_1, r_2, \ldots, r_N]$
Output M {**M** is a $L \times p$ estimated mixing matrix}
1: $\mathbf{R}_p := \mathbf{U}_p^T \mathbf{R}_0$; {$\mathbf{U}_p$ obtained by SVD, and $\mathbf{R}_0$ is the zero-mean of $\mathbf{R}$}
2: indice := randi(N,p); {indice is the randomly selected p points from N samples}
3: $\mathbf{R}_{aux} := [\mathbf{R}_p]_{:,indice}$;
4: max_vol := det($\mathbf{R}_{aux}$);
5: **for** $i := 1$ to N **do**
6:      $\mathbf{r} := [\mathbf{R}_p]_{:,i}$;
7:      **for** $j := 1$ to p **do**
8:          $[\mathbf{R}_{aux}]_{:,j} := \mathbf{r}$; {temporarily updates the jth endmember}
9:          vol_aux := det($\mathbf{R}_{aux}$);
10:         **if** vol_aux > max_vol **then**
11:             max_vol := vol_aux;
12:             indice$_j$:= i;
13:         **end if**
14:     **end for**
15: **end for**
16: $\mathbf{M} := \mathbf{U}_p[\mathbf{R}_p]_{:,indice}$;

3.2.3 Vertex Component Analysis (VCA): A Fast Algorithm to Unmix Hyperspectral Data

The vertex component analysis (VCA) [43] algorithm is based on the assumption that the endmembers are the vertices of a simplex. The data is carried in this simplex of minimum volume. The algorithm iteratively projects data onto a direction orthogonal to the subspace spanned by the endmembers already determined. The new endmember signature corresponds to the extreme point of the projection. The algorithm iterates until all endmembers are exhausted (p). The pseudo code of the algorithm is given in Algorithm 3. VCA is one of the mostly preferable geometrical approaches in the literature due to its simplicity, low number of iterations and high accuracy.

Algorithm 3 Vertex Component Analysis (VCA)[43]

Input p, $\mathbf{R} \equiv [r_1, r_2, \ldots, r_N]$
Output M $\{\mathbf{M}$ is a $L \times p$ estimated mixing matrix$\}$

1: $\mathbf{X} := \mathbf{U}_p^T \mathbf{R}; \{\mathbf{U}_p$ obtained by SVD$\}$
2: $\mathbf{u} := \text{mean}(\mathbf{X}); \{\mathbf{u}$ is a $1 \times p$ vector$\}$
3: $[\mathbf{Y}]_{:,j} := [\mathbf{X}]_{:,j} / [\mathbf{X}]_{:,j}^T \mathbf{u}; \{$projective projection$\}$
4: $\mathbf{A} := [e_u | 0 | \ldots | 0]; \{e_u = [0, \ldots, 0, 1]^T$ and $\mathbf{A}$ is a $p \times p$ auxiliary matrix$\}$
5: **for** $i := 1$ to p **do**
6: $\quad \mathbf{w} := \text{randn}(0, \mathbf{I}_p); \{\mathbf{w}$ is a zero-mean random Gaussian vector of covariance $\mathbf{I}_p\}$
7: $\quad \mathbf{f} := ((\mathbf{I}\text{-}\mathbf{A}\mathbf{A}^{\#})\mathbf{w})/(\|(\mathbf{I}\text{-}\mathbf{A}\mathbf{A}^{\#})\mathbf{w}\|); \{\mathbf{f}$ is a vector orthonormal to the subspace spanned by $[\mathbf{A}]_{:,1:i}\}$
8: $\quad \mathbf{v} := \mathbf{f}^T \mathbf{Y};$
9: $\quad k := \text{argmax}_{j=1,\ldots,N} |[\text{v}]_{:,j}|; \{$find the projection extreme$\}$
10: $\quad [\mathbf{A}_{:,i}] := [\mathbf{Y}_{:,k}];$
11: $\quad [indice]_i := \text{k}; \{$stores the pixel index$\}$
12: **end for**
13: $\widehat{\mathbf{M}} := \mathbf{U}_p[X]_{:,indice};$

A sample run is performed to illustrate the iterations of the algorithm (see in Figure 8). The extreme points are the maxima of $\mathbf{v}$ (projection vector), and the vertices of the hyper plane are computed by updating $\mathbf{A}(p \times p)$ after each iteration. $\mathbf{A}$ is an auxiliary matrix which stores the projection of the estimated endmembers signatures. The *indices* of the extreme points are stored, and the spectra corresponding to these indices in data $\mathbf{R}(p \times L)$.

3.3 Spatial-Spectral Unmixing Approaches

Bioucas-Dias et al. [38] indicate in their review that statistical models are powerful alternatives when the spectral mixtures are highly mixed. However, statistical models come with higher computational complexity compared to the geometrical models. Another approach in unmixing literature is the incorporation of spatial information into the spectral unmixing. As it is discussed in [38], the geometrical, statistical and

20

sparsity-based approaches work on spectral domain, and ignore the valuable information in spatial domain. Researchers are motivated to classify hyperspectral images by exploiting the correlation between both spatial and spectral neighbors. The idea in this approach is to utilize the spatial information in addition to the spectral unmixing algorithms at the expense of additional computation cost. The review of hyperspectral unmixing covers several methods in both endmember extraction and abundance estimation steps that take advantage of 3D structure of hyperspectral cube.

In the proposed catadioptric hyperspectral imaging system, we aim to utilize the difference in spatial resolution between the center and outer parts of the mirror and furthermore to account for the distortion in the mirror. As the spatial resolution increases toward the image center, the possibility of detecting pure pixels in the outer regions of the image increases. Therefore, the spatial-spectral unmixing approaches are reviewed in this chapter. Xu et al. [44] and Yan et al. [45] fuse spatial and spectral information in a sub-pixel level. Yan et al. [45] divide a pixel into sub-pixels which are redefined by the scalar factor related to the spatial-spectral similarity. Xu et al. [44] use sub-pixels in the derivation of fractional abundance maps.

Automated Morphological Endmember Extraction (AMEE) [46], Spatial Preprocessing for Endmember Extraction (SPP) [47], Region-based spatial preprocessing (RB-SPP) [48] and Spatial-Spectral Preprocessing (SSPP) [49] are well known spatial-contextual unmixing algorithms. These algorithms are reviewed in the following subsections.

Xu et al. [44] and Yan et al. [45] perform a sub-pixel spectral mixture analysis. AMEE and SPP are pixel-based unmixing approaches, and RBSPP and SSPP are region-based approaches. In the proposed system, the endmembers are extracted from the individual regions which are partitioned according to their spatial resolutions. Therefore, region-based unmixing approaches are more related with the proposed study. Martin and Plaza proposed an improved version of RBSSP in SSPP. Hence, the proposed algorithm is only compared with SSPP based on the experimental results presented in their study.

3.3.0.1 Automated Morpholocial Endmember Extraction (AMEE)

AMEE [46] is one of the first attempts of incorporating spatial information in spectral unmixing. The conventional morphological operations are extended to the multidimensional data. The algorithm is based on the Morphological Eccentricity Index (MEI) which is the distance measure between the neighbors. Figure 9 illustrates the flowchart of the AMEE algorithm. The kernel is moved through all the pixels of the image. The spectrally purest pixel and the spectrally most mixed pixel at each kernel neighborhood are obtained by multidimensional dilation and erosion operations. Grayscale dilation and erosion algorithms are expanded to multi-dimensional space. These morphological operations iterate from pre-defined minimum window size to maximum window size. These values are arranged according to the optimum range for performance and cost. They use Spectral Angle Distance (SAD) as pointwise dis-

tance measure. The "eccentricity" of a pixel points its distance to the spectrally pure or most highly mixed element. They propose that this index can be used as an important indicator to determine the pixel purity degree. After morphological operations, the MEI map of the hyperspectral data is generated.

Automated endmember selection is performed by using the MEI map. It is obtained in the competitive endmember selection step by using a threshold. In the algorithm, a multilevel Otsu thresholding [50] method is used in order to define the threshold value. After thresholding the MEI image, the regions corresponding to the endmember candidates are generated by using a region growing algorithm. In this step, another threshold for region growing is used to add sufficiently similar pixels to the regions. After the region growing process, the mean spectra of the final regions are obtained. As a consequence, a final endmember set is obtained. The need for two threshold values and the cost of iterative processes for different window sizes limit the effectiveness of the algorithm.

As AMEE is one of the first attempts of spatial-contextual unmixing approach. More robust and high performance methods are developed in the following years.

3.3.0.2 Spatial Preprocessing for Endmember Extraction (SPP)

Zortea and Plaza [47] present a similar approach to AMEE algorithm related with the incorporation of spatial information. A kernel moves over the hyperspectral image to compute a scalar. The scalara value corresponds to the spectral similarity of pixels lying within a certain spatial neighborhood. The Spatial Preprocessing for Endmember Extraction (SPP) algorithm differs in taking into consideration the spatial distance of each pixel in the kernel. By this way, the similarity measures are also weighted according to their spatial distances to the center of the kernel. The similarity of adjacent pixels has higher importance.

They categorize four types of pixels according to both spectral and spatial properties. Spectrally pure and mixed pixels are defined as made up of a single and several spectral signatures, respectively. On the other hand, spatially homogeneous pixel defines a pixel whose spectral signature is similar to its surrounding pixels. The last category covers the anomalous pixels which can be considered as the opposite of spatially homogeneous pixels. It should be noted that homogenous and anomalous pixels may or may not be pure. However, homogeneous areas provide good candidate pixel vectors for endmember extraction. The transition areas between neighboring objects contain most probably mixed pixels. Conversely, the pure pixels correspond to the endmembers less likely exist in these areas.

SPP is not an endmember extraction algorithm. It is proposed as a preprocessing algorithm for the endmember extraction algorithms. The image is modified according to the weighting factor, and the output is sent as an input to an endmember extraction algorithm. The main idea of the algorithm is to estimate the scalar weighting factor $\alpha(i, j)$ for each pixel in the image where (i, j) is the center pixel in a square shaped

spatial region with a size of $ws \times ws$. The weighing factor is computed as follows:

$$\boldsymbol{\alpha}(i,j) = \sum_{r=i-d}^{i+d} \sum_{s=j-d}^{j+d} \beta(r-i, s-j)\gamma(r-i, s-j) \tag{19}$$

$$\gamma(r-i, s-j) = \gamma(\mathbf{X}(r,s), \mathbf{X}(i,j)) \tag{20}$$

where $\mathbf{X}$ is the three dimensional hyperspectral data cube, γ refers to a similarity measure calculated between the central pixel $\mathbf{X}(i,j)$ and the neighboring pixel $\mathbf{X}(r,s)$. β is a scalar value that weights the spatial closeness between pixels.

$$\rho(i,j) = (1 + \sqrt{\alpha(i,j)})^2 \tag{21}$$

$$\mathbf{X}(i,j)' = \frac{1}{\rho(i,j)}(\mathbf{X}(i,j) + \bar{\mathbf{I}}) + \bar{\mathbf{I}} \tag{22}$$

where the term $\mathbf{X}(i,j)'$ denotes a spectral signature obtained after weighing $\mathbf{X}(i,j)$ using spatial information, and $\bar{\mathbf{I}}$ is the centroid of the data cloud, which was computed as the mean of all the pixel vectors in the original hyperspectral scene $\mathbf{I}$.

The strategy of SPP is based on a spatial window which translates over the spatial domain of the scene in order to investigate contextual information around image pixels. This is feasible for the scene where the spatial variation is smooth. However, for the discontinuities and fast changing of spectral information, a region-based adaptive method is developed.

3.3.0.3   Region-based spatial preprocessing (RBSPP)

Region-based spatial preprocessing (RBSPP) [48] uses the spatial information as a guide in order to extract the spectral information more effectively. The algorithm adequately exploits the spatial context in an adaptive manner. This approach first searches for the spectrally pure regions. In othe words, it searches the groups of several contiguous pixel vectors having similar spectral content. The algorithm use a hybrid procedure that combines unsupervised clustering and orthogonal subspace projection concepts. Then, the method performs unsupervised clustering by using the ISODATA [51] algorithm. Finally, the algorithm applies the orthogonal subspace projection to the mean spectra of the resulting regions. The projection is performed in order to find a set of spatially representative regions with associated spectra which are both spectrally pure and orthogonal between them. Furthermore, a spectral-based endmember estimation algorithm can be applied to the pixels in the resulting spatially connected regions. The flowchart of the algorithm is provided in Figure 10.

RBSPP is a region-based method contrary to the pixel-based ones which are previously discussed in spatial-contextual methods. As, it discards a high number of pixels, the total endmember extraction processing time significantly decreases.

3.3.0.4 Spatial-Spectral preprocessing (SSPP)

Spatial-Spectral preprocessing (SSPP) [49] is also a similar approach to RBSPP. It considers spatial and spectral information simultaneously and fuses both sources of information at the preprocessing level. The flowchart of the algorithm is provided in Figure 11. The algorithm consists two pixel-based steps. First, the hyperspectral image is filtered by a multi-scale spatial Gaussian filter. A spatial homogeneity index is computed by using the difference between the original and filtered hyperspectral image. Consequently, similar to the PPI algorithm, a spectral purity index is defined. A principal components transformation is performed. The weight of the maxima and minima of the projection are one, and the weight of the mean of the projection is zero. The sum of all weights for a pixel defines its spectral purity index. Two threshold values are used for spatial and spectral analysis in order to discard lower indices. In parallel to the first two steps, an unsupervised spectral clustering algorithm (ISODATA [51]) is performed. The rest of the algorithm is region-based. The regions with high spectral purity and high spatial homogeneity are selected. The endmember selection process is only performed on these selected regions. Therefore, the processing time of the endmember estimation process significantly decreases. According to the experimental results provided by Martin and Plaza, SSPP produces more robust results than RBSPP.

3.4 Abundance Estimation of the Endmembers

For some unmixing applications, it is sufficient to only estimate the endmember signatures. However, for some applications, the abundances of endmembers, in sub-pixel manner, is also desired information. Several least squared error based algorithms are proposed in the literature for this purpose. These algorithms vary according to their constraints, and Table 1 shows the related algorithms.

Table 1: Least Squared Error Based Abundance Estimations Algorithms

	Non-Negativity Constrained (✓)	Non-Negativity Constrained (✗)
Sum-to-One Constrained (✓)	NSCLS [52] FCLS [53]	SCLS [54]
Sum-to-One Constrained (✗)	NCLS [55]	

The proposed system in this study needs to be employed both of the constraints listed above. We use a fast non-negativity constrained least squares algorithm [56], and then we normalized the abundances so that sum-to-one constraint is satisfied.

An experiment is performed to visualize the abundance estimation approach in unmixing problem. The scene is composed of the materials with distinctive spectral characteristics in visible and near-infrared (VNIR) region of electromagnetic spec-

trum. The scene is composed of bone, soil, and vegetation residue that can be dealt with in food inspection and archaeological remote sensing applications. We perform measurements on bone samples by using ASD spectrophotometer in 350 nm – 2500 nm. Figure 12 depicts the captured signals from raw and cooked bones. The significant absorption peaks correspond to hemoglobin (540 nm – 580 nm), water (978 nm, 1192 nm, 1464 nm, and 1930 nm) and lipid (1745 nm) contamination [57], [58]. The hyperspectral camera used in our experiments is able to measure the range of 400 nm - 1000 nm. The hemoglobin contamination of the bone is a significant indicator in VNIR imaging.

Vegetation also demonstrates distinguishable reflectance characteristic in electromagnetic spectrum. A healthy vegetation shows a sharp increase in red edge region due to its chlorophyll content. The high absorption in red region and high reflectivity in near infrared region cause a significant difference in vegetation spectra. Therefore vegetation indices are mostly preferred in detection, identification and classification problems of the hyperspectral data.

Figure 13 shows the scene composed of vegetation, soil, bone sample, white paper, white reflectance, black reflectance, checkboard, building, and sky. Figure 13b is the cropped region to be studied that contains vegetation, soil, bone samples, white paper, and sky in the background. The spectral resolution of the data 0.73 nm, and the spatial resolution is 0.9 mm for the outer part and 3.3 mm for the inner part approximately.

Figure 14 illustrates the estimated endmembers by VCA algorithm. The blue signature (endmember #1) with the higher reflectivity is most likely belongs to the white paper. The green signature (endmember #2) shows a sharp increase in near-infrared (NIR) region, and it belongs to vegetation. The endmember #4 and #5 have low reflectivity roughly in 540 nm and 580 nm. These dips are related with the hemoglobin content of the bone samples as discussed in the previous subsection. As the scene is observed, the last endmember must be belong to sky or soil endmember. However, the pixels corresponding to the sky have low reflectivity due to low incident light. The soil, sky, and shadowy pixels are estimated in an only endmember (endmember #3). Figure 15 visualizes the abundances of estimated endmembers in the image. The red and white parts of the bones are estimated separately. The red bone samples reflect the incident light comparatively higher between 600 nm – 700 nm (Figure 14 endmember #4 and #5).
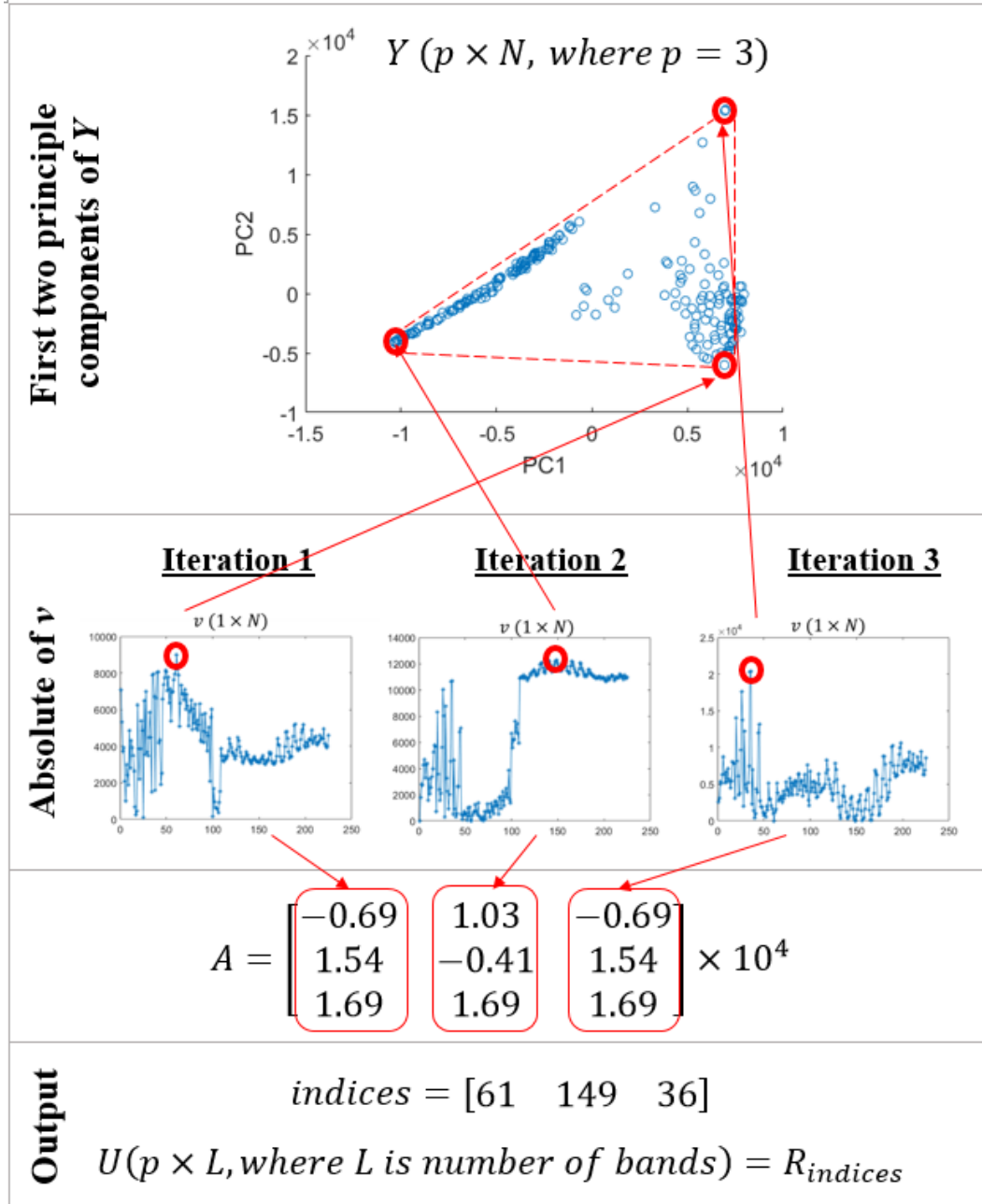
Figure 8: An example illustration for VCA iterations.
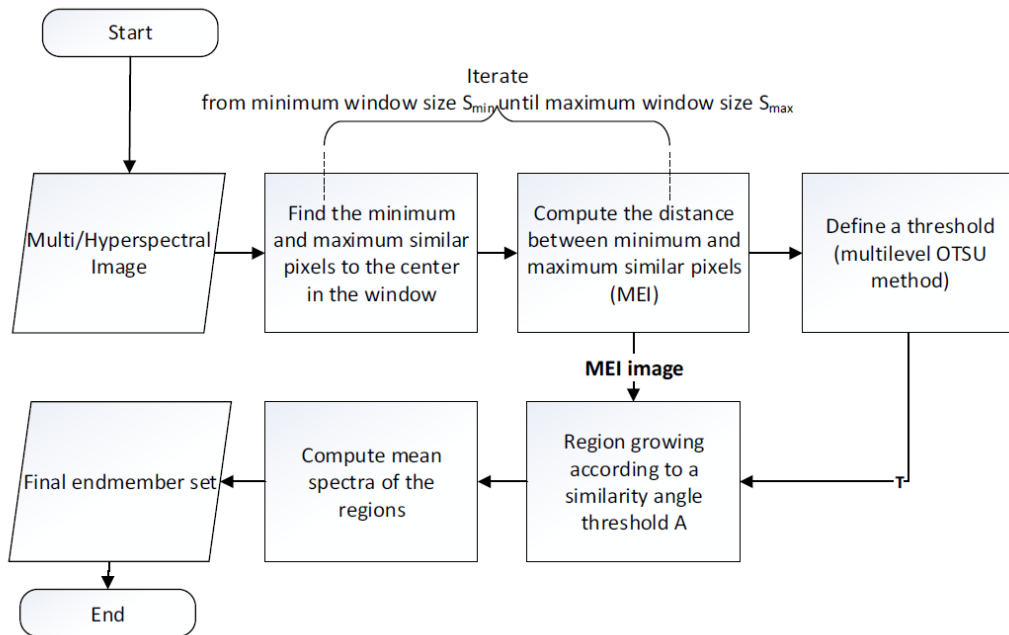
Figure 9: Flowchart of AMEE algorithm.
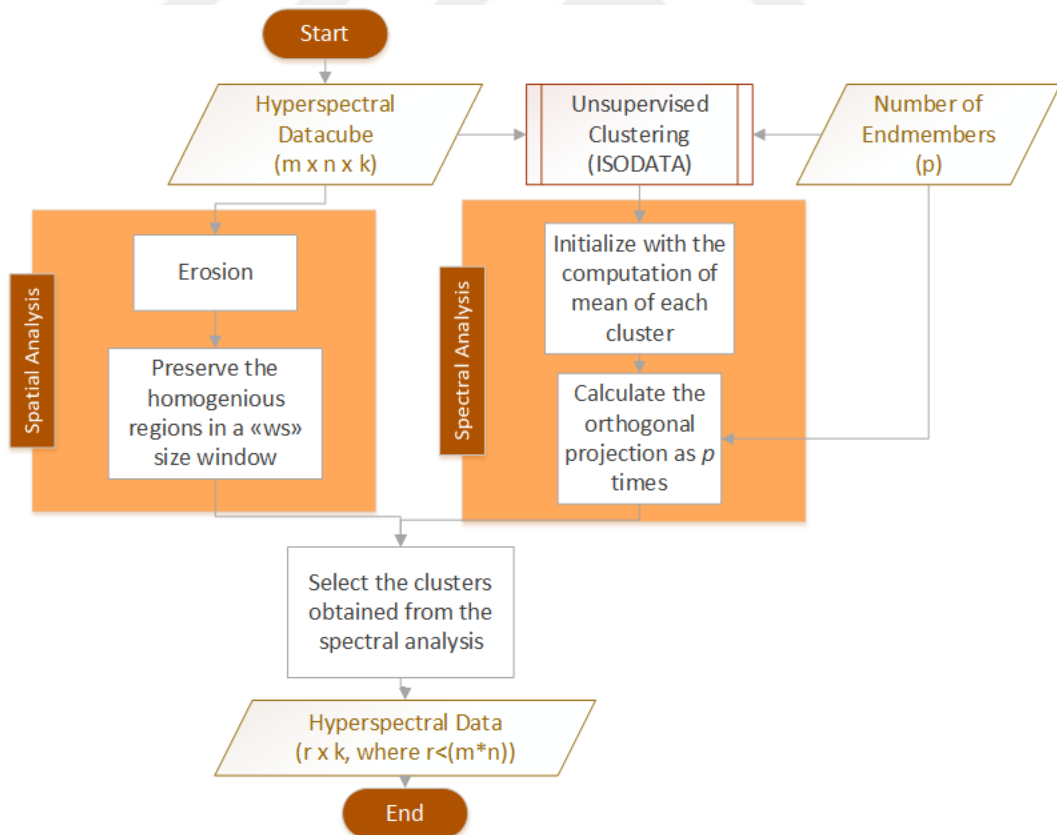
Figure 10: Flowchart of RBSPP algorithm.
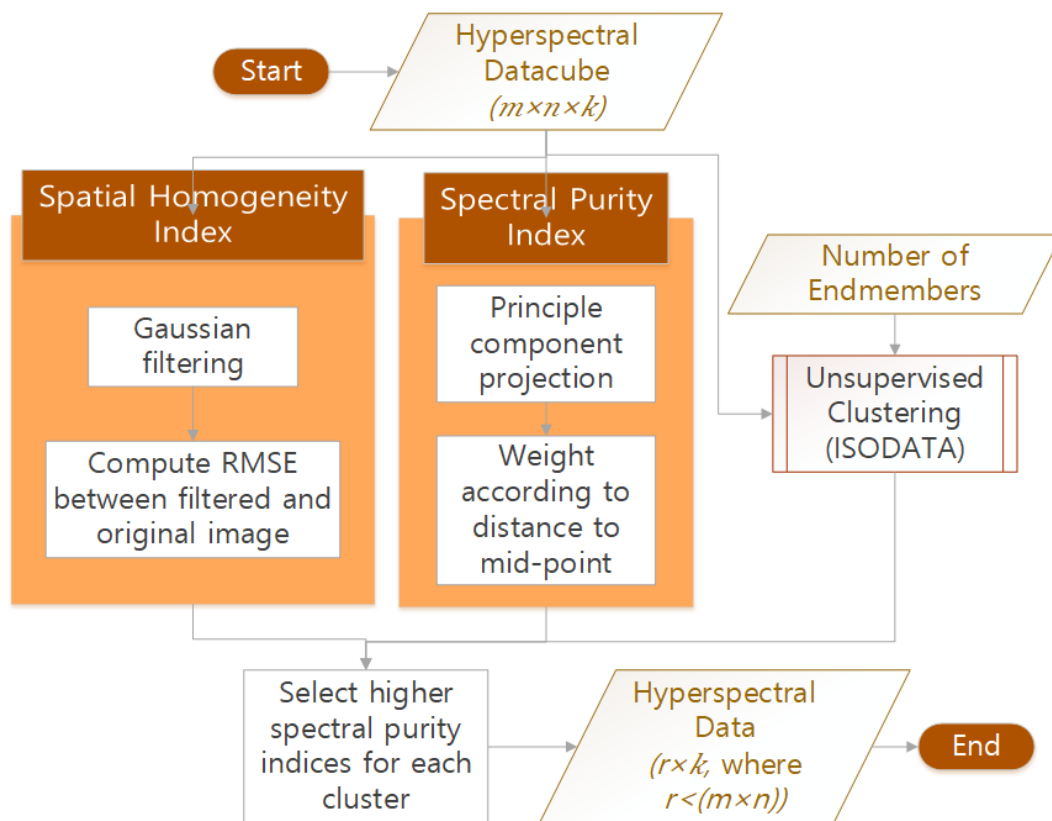
Figure 11: Flowchart of SSPP algorithm.
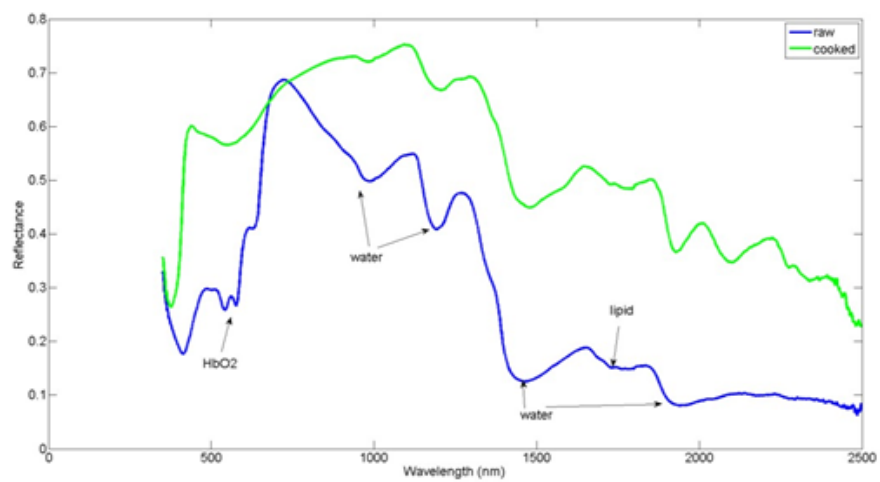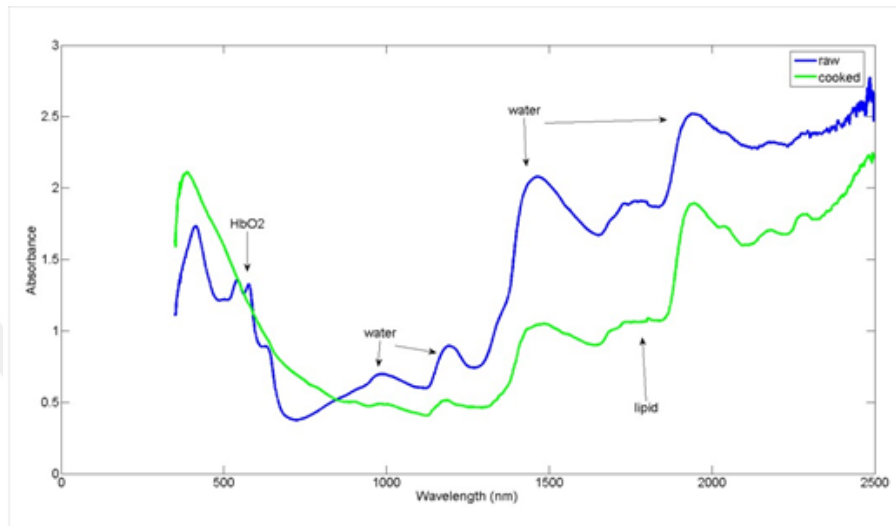
Figure 12: Bone absorbance (a) and reflectance (b) spectra, respectively.
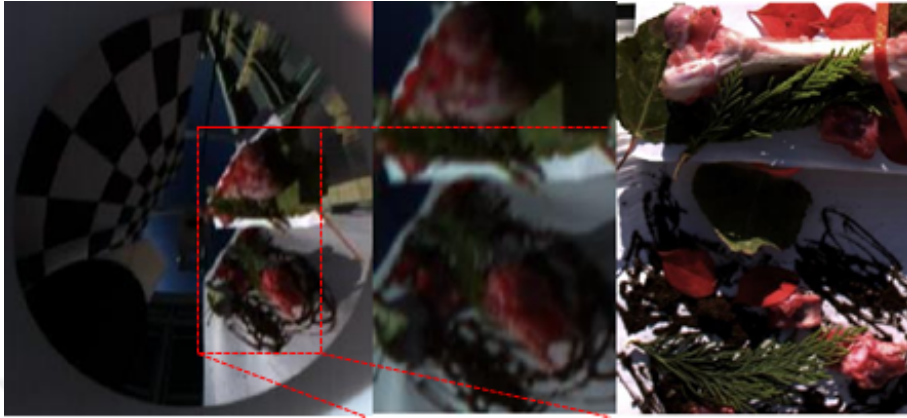
Figure 13: RGB representation of data. (a) Omnidirectional image. (b) In-zoom demonstration of region of interest. (c) The RGB image of the corresponding region acquired by area scan camera.
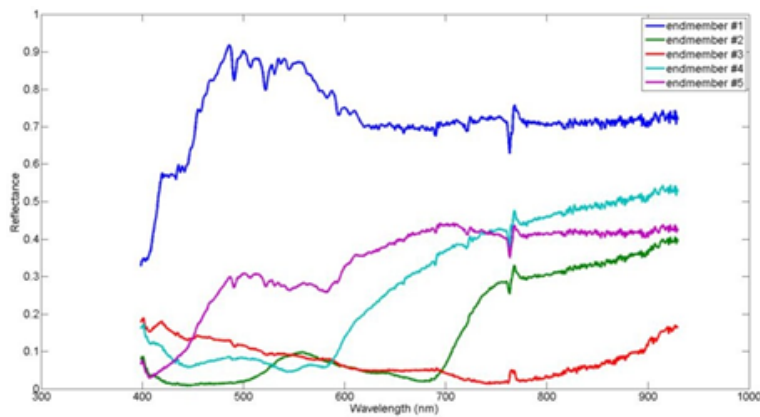
Figure 14: Estimated endmember spectra by VCA.
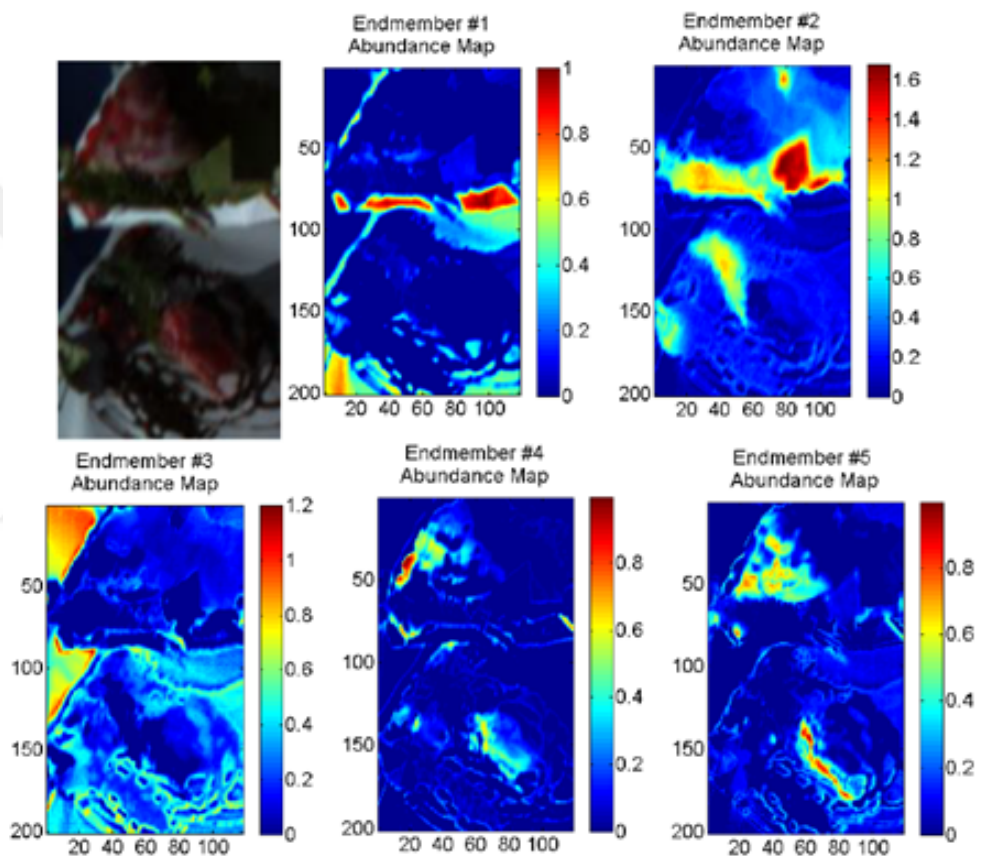
Figure 15: Estimated abundance maps for each endmember given in Figure 14.

CHAPTER 4

PROPOSED METHOD

In the Proposed Method Chapter, the preprocessing steps and the proposed improvements are explained. The novel approaches which are specially investigated for the proposed catadioptric hyperspectral imaging system are presented. Spectral signature mixing is a commonly encountered problem caused by low spatial resolution in hyperspectral imagery. It becomes a more challenging problem in omnidirectional images. Objects are represented with fewer number of pixels by the side of the mirror center due to the mirror shape. This deformation can be seen in Figure 16. The reduction in the spatial resolution causes mixed pixels to be located around the mirror center. In this dissertation, we aim to propose the application of approaches which take into consideration the locations of the pixels on the mirror. A general flowchart of the algorithm is given in Figure 17.

Figure 16: An example for the distortion on omnidirectional images.

4.1 Preprocessing

A preprocessing step is required for real world acquisitions. First, the raw data gathered from the camera is converted to the reflectance unit. The data is effected by the camera parameters and the illuminator's spectral characteristics. Hyperspectral
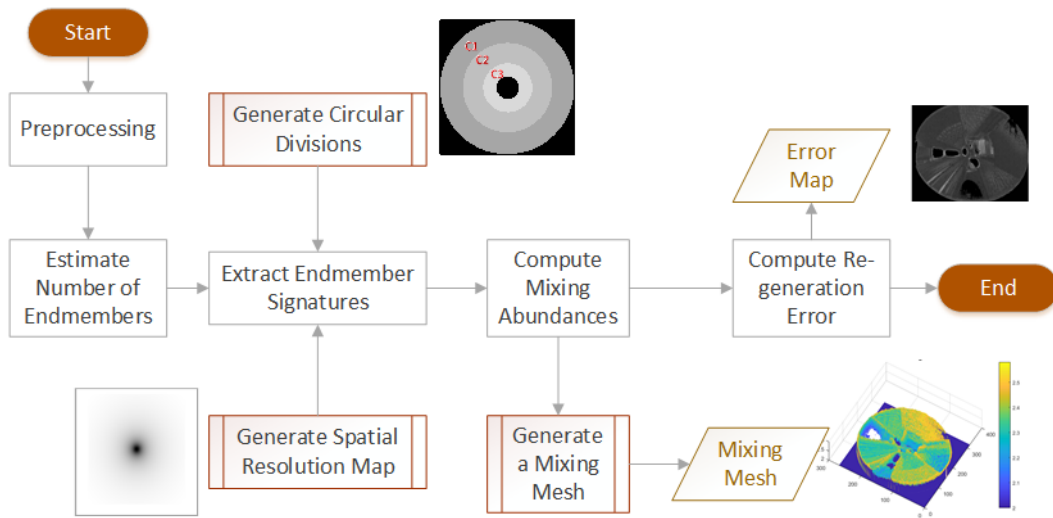
Figure 17: Flowchart of the general unmixing approach.

sensor is calibrated by using the objects having highest and lowest intensity values that might be exist in the scene. This process helps to create the intensity range of the scene. In our experiments, we use a black object as a dark reference, and a plate made of teflon as white reference which has high reflectivity in VNIR region. However, the pixels with higher intensity values than white reference, cause to occur the saturated pixels. In the experiments performed in this study, the reflected light from the aluminum pole, surrounding buildings, and the sky are saturated. The algorithms explained in Section 3.2 aim to detect extreme points of the simplex. In that case, the saturated pixels are always detected as the endmembers. In order to prevent this case, the pixels having higher reflectivity than a hundred percent are ignored. Lastly, the outside of the mirror area is blocked in order to exclude from the unmixing analysis. The flowchart of the algorithm is provided in Figure 18.

4.2 Spatial Resolution Factor

The spatial resolution factor is derived in Eq. 11. However, in the implementation phase, the expression needs to be represented in terms of image point coordinates. The relation between mirror parameters, image point coordinates and 3D outgoing ray are explicitly set up by Onoe et al. [33]. The study generates panoramic and perspective images from omnidirectional video streams. It describes an approach on acquisition an omnidirectional video by using the HyperOmni Vision system. The setup is mounted on a car, and it uses a hyperboloidal mirror which is abbreviated in the name of the system. The developed system is composed of two steps: video-rate omnidirectional image acquisition and perspective image generation from an omnidirectional video stream. We widely use their explanations on computation of the resolution factor and generation of the simulated data.

34
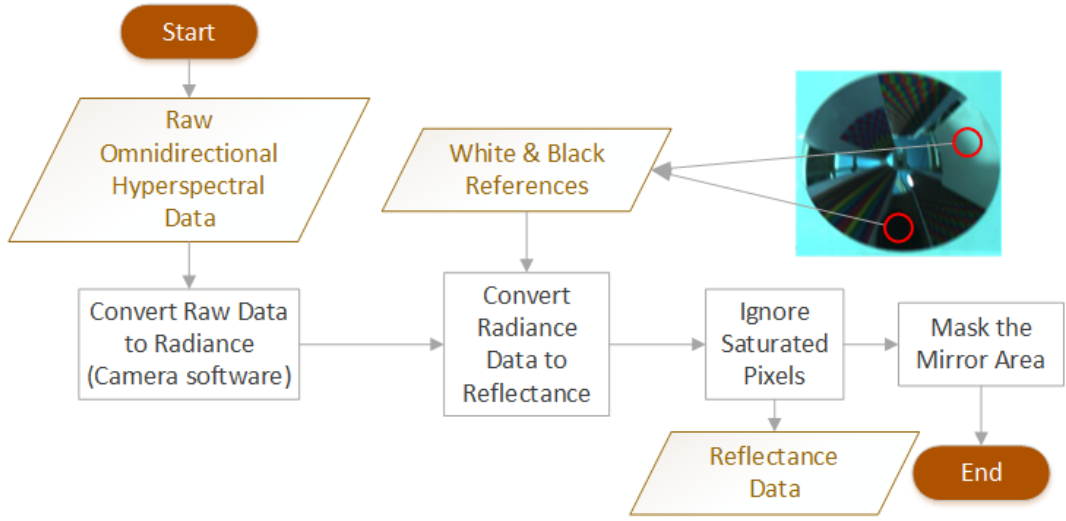
Figure 18: Flowchart of the preprocessing.

As illustrated in Figure 6 (Section 2.3), a ray coming from the world point $P(X, Y, Z)$ toward the focal point v of the hyperboloidal mirror is reflected by the mirror and passes through the other focal point (camera center) p, and the ray intersects an image plane at a point (x, y). This hyperboloidal projection yields the equations in [33] as:

$$\theta = \tan^{-1} \frac{Y}{X} = \tan^{-1} \frac{y}{x} \tag{23}$$

$$\gamma_c = \tan^{-1} \frac{u}{\sqrt{x^2 + y^2}} \tag{24}$$

$$\gamma_m = \tan^{-1} \frac{(b^2 + (c/2)^2) \sin \gamma_c - 2b(c/2)}{(b^2 - (c/2)^2) \cos \gamma_c} \tag{25}$$

where (x, y) are the image point, and u is the focal length of camera lens (the distance between the point p and the image plane). On the other hand, Baker and Nayar [32] present the relation between the mirror angle (γ_m) and the mirror points:

$$\tan(-\gamma_m) = \frac{z}{r} \qquad \tan(\gamma_c) = \frac{c - z}{r} \tag{26}$$

By using the equations between (24-26), r and z can be re-written as:

$$r = \frac{c}{\tan(-\gamma_m) + \tan(\gamma_c)} \qquad z = \tan(-\gamma_m)r \tag{27}$$

The illustrations about the relation between the pixel coordinate and the spatial resolution are presented in the following part of this section.

1. We performed several studies in order to show the change on spatial resolution of the omnidirectional image. These studies also aim to demonstrate the spatial

Figure 19: (a) Spatial resolution map (The values are presented in grayscale). (b) Resolution factors of the pixels at the corresponding line in (a). (c) Front view of the simulated scene. (d) Omnidirectional image. (e) The radial distortion on checkerboard.

distortion occurred due to the mirror shape. First, we simulate the image which is generated according to the coordinate system of an omnidirectional imag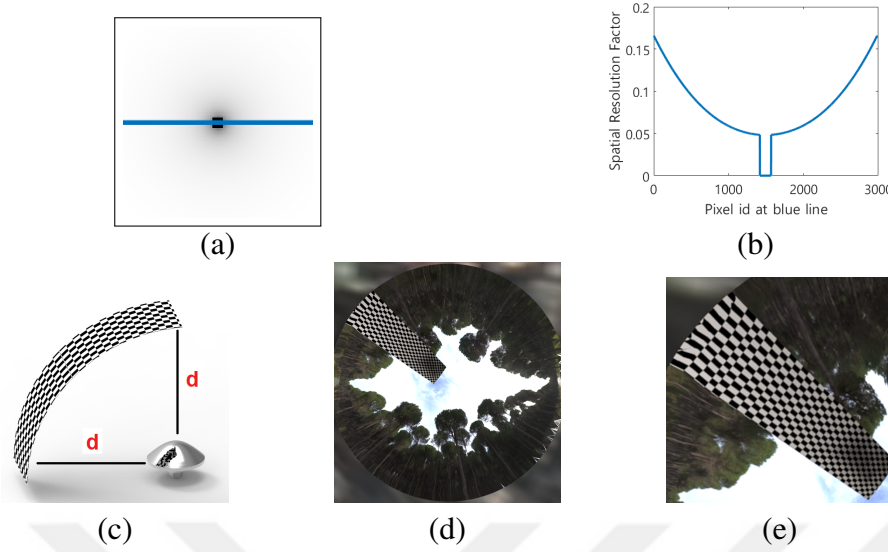e. The mirror parameters are selected the same with NeoVision hyperbolic mirror ($a = 28.095, b = 23.4125$). Figure 19a illustrates the change on the resolution of the simulated omnidirectional image in grayscale format where dark colors imply the lower spatial resolution values. This illustration helps us to make an inference about the decrease of the spatial resolution through the mirror center. The range of the resolution values are plotted in Figure 19b. For an image with size of (164×164), the resolution factors vary to values between 5.52 and 0.3813. After masking the camera location in the center of the image, the resolution factors vary to values between 5.5 and 3.2.

2. One of the research questions of this study period is to investigate whether the resolution factor is dependent on the distance between object and mirror. The objects surrounding the mirror are naturally perpendicular to the ground. For this case, the distance between object and mirror increases through the z direction.

The distance d shown in Figure 19c is equal for the upper and bottom part of the checkerboard. In this experiment, while preserving the distance to mirror on each point of the object, we still observe the distortion and the change on the resolution.

These experiments show that the resolution factor changes regardless of the distance between object and mirror. The only parameter that effects the formula of the resolution factor is the r coordinate of the mirror point.

4.3 Proposed Improvement on Geometrical Unmixing Approaches (Omni-Approach)

The method that we propose is similar to the conventional spatial-spectral unmixing approaches in terms of requiring a preprocessing step before endmember estimation. However, unlike these methods, it does not require spatial connectivity. It aims to overcome the inequality of spatial resolution that occurs in the omnidirectional hyperspectral image. In the preprocessing step, the spatial resolution map is generated by using the camera and mirror parameters (explained in Section 4.2). In this respect, the preprocessing step proposed in this study is independent from the scene content. Then, the map is integrated to the endmember estimation algorithm to be applied. Therefore, the effect on the endmember estimation algorithm is negligible in terms of processing time. This provides a great advantage compared to the other spatial-spectral unmixing methods. The complexity of the proposed algorithm is $O(n)$ where n is $row \times column$ of the omnidirectional image.

The methods that are evaluated in this study are geometry based approaches and they aim to extract the endmember signatures by maximizing the volume. Under the assumption that the endmembers must be located at the extrema, the data is multiplied by the spatial resolution map just before detecting the maxima of the volume (see in Table 2). Thus, the point having high spatial resolution is translated to outer of the simplex. The possibility of detecting a point having higher spatial resolution as an extreme point is increased in this way. Conversely, the pixel with lower resolution is forced to translate to inner position in the data cloud. The maxima of the algorithms are evaluated in the 6. line of PPI (Algorithm 1), 10. line in N-FINDR (Algorithm 2), and 9. line in VCA (Algorithm 3). We propose to perform the multiplication just before the measuring the maximum of the data (see in Table 2).

Table 2: The Proposed Omni-Approach on Geometrical Unmixing Algorithms

	Original Geometrical Unmixing Algorithm	**Omni-Approach**
PPI	$[max\_vol, idx] := max(vol\_aux)$	$[max\_vol, idx] := max(vol\_aux * res\_factor)$
N-FINDR	$vol\_aux := det(R_{aux})$	$vol\_aux := det(R_{aux} * res\_factor)$
VCA	$k := argmax_{j=1,...,N}|[v]_{i,j}|$	$k := argmax_{j=1,...,N}|[v * res\_factor]_{i,j}|$

4.4 Proposed Improvement on Spatial-Spectral Unmixing Approaches

The main idea of the algorithm is to estimate the scalar factor $\rho(i,j)$ for each pixel in the image. $\mathbf{X}(i,j)$ is the center pixel in a square-shaped spatial region with a size of $w \times w$. The weighing factor $\alpha(i,j)$ is computed as shown in Line 2 in Table 3. γ refers to a similarity measure calculated between the central pixel $\mathbf{X}(i,j)$ and the

Table 3: SPP Algorithm

1	$d = \frac{w}{2}$
2	$\boldsymbol{\alpha}(i,j) = \sum_{r=i-d}^{i+d} \sum_{s=j-d}^{j+d} \beta(r-i, s-j)\gamma(r-i, s-j)$
3	$\gamma(r-i, s-j) = \gamma(\mathbf{X}(r,s), \mathbf{X}(i,j))$
4	$\beta(i,j) = \frac{1}{\sqrt{i^2+j^2}}$
5	$\rho(i,j) = (1 + \sqrt{\boldsymbol{\alpha}(i,j)})^2$
6	$\mathbf{X}(i,j)' = \frac{1}{\rho(i,j)}(\mathbf{X}(i,j) - \bar{\mathbf{I}}) + \bar{\mathbf{I}}$

neighboring pixel $\mathbf{X}(r,s)$. β is a scalar value that weights the spatial closeness between pixels. The term $\mathbf{X}(i,j)$' denotes a spectral signature obtained after weighing $\mathbf{X}(i,j)$ using spatial information, and $\bar{\mathbf{I}}$ is the centroid of the data cloud, which was computed as the mean of all the pixel vectors in the original hyperspectral scene $\mathbf{I}$.
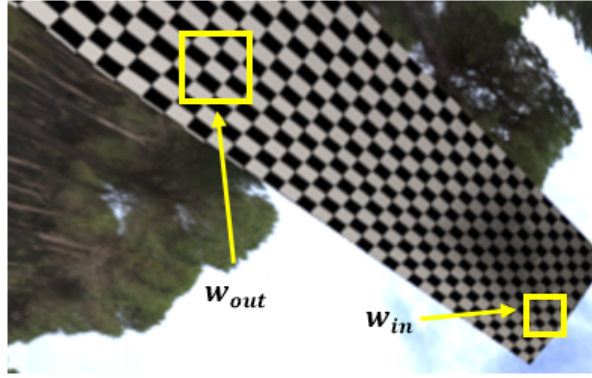
Figure 20: Inner and outer windows (w_{in}, w_{out}) capture same spatial size in real world.

$$\frac{w_{in}}{w_{out}} = \frac{res_{in}}{res_{out}} \tag{28}$$

$$\frac{\beta(r_{in} - i_{in}, s_{in} - i_{in})}{\beta(r_{out} - i_{out}, s_{out} - i_{out})} = \frac{res_{out}}{res_{in}} \tag{29}$$

where w_{in} and w_{out} are the window size, and res_{in} and res_{out} are the spatial resolutions for the corresponding locations. The window size w (Table 3 – Line 1) must be set according to the ratio between the corresponding spatial resolutions. In Figure 20, w_{in} and w_{out} contain same spatial area in real world, four black squares on checkerboard. However, it is explicitly seen in the figure that the pixel size of the windows on omnidirectional image are quite different.

Additionally, the SPP approach is based on the spatial equality of the image pixels. It means that each pixel in the image has the same spatial resolution. However, the omnidirectional image formation contains different spatial resolutions. Therefore, the spatial distance measured in β function must be computed according to the spatial resolution ratio between inner and outer parts (Eq. 29).

4.5 Proposed Local Endmember Extraction Approach on Omnidirectional Images

The materials present in the scene may have diversity on their spectral characteristics, even though they are pure pixels conceptually. Different environmental and illumination conditions such as shadow of an object and heterogeneous content of the material cause a variety on the pure spectral signatures of the material. A single representer for each class for the complex unmixing problem may not be found. For these reasons, some researchers prefer to conduct their unmixing studies on local endmember estimation approach [59, 60]. This approach investigates the spectral unmixing algorithms in a small size window independently from the rest of the scene. Somers et al. [59] introduced a similar algorithm. They select subsets from the hyperspectral data cube. The extracted endmembers from the subsets are stored in a global endmembers set, and then clustered in order to obtain the global representers of the pure materials. This algorithm is also used in [60], which aims to monitor seasonal variations of vegetation cover. They estimate the abundances of the endmembers with a different viewpoint. The data cube is evaluated using the global endmembers set, then the abundances of the endmembers belonging to the same cluster are accumulated for each pixel. As a conclusion, they indicate that the local unmixing idea benefits to discriminate two similar vegetation species.

In our study, we propose that spectral analysis of partitioned circles which are generated according to their spatial resolution factors, is more appropriate for omnidirectional hyperspectral images. The materials with different spatial resolutions may have a diversity on their spectral signatures. Local unmixing approach prevents to miss these cases. The scheme of the proposed algorithm is depicted in Figure 21. The image is divided into three circles with equal number of pixels. The estimation of number of endmembers and estimation of spectral signature of endmember (EEA) are studied independently on each circle. The first column depicts the estimated pure pixel locations with red dots on the image, their corresponding spectra are plotted in the following column. After endmember estimation, a bundle of endmembers is accumulated. The studies presented in [59], [60] take advantage of high number of endmembers by using Multiple Endmember Spectral Mixture Analysis (MESMA) [61]. The algorithm is based on using a library which contains field and laboratory measurements. An enhanced performance of MESMA is presented at [62]. A wide range of instances according to the application is collected. In spectral mixture analysis, it achieves to discriminate similar spectra [61]. In the proposed algorithm, we do not use such a library. Instead, we use the internal information of the hyperspectral data as it is proposed in the study of Somers et al.. A library is created by collecting from endmember estimation of each circular sub-region. The collected endmembers set is clustered by k-means[63], and an optimal abundance map is computed by using multiple endmember spectral mixture analysis. The last column consists the clustered endmembers and the error maps where white color indicates higher error. The definition of error map is presented in Section 5.2.1. Note that, the proposed method is combined with the improvement explained in Section 4.3. The pixels in the circular sub-regions are multiplied with their corresponding spatial resolution factor.
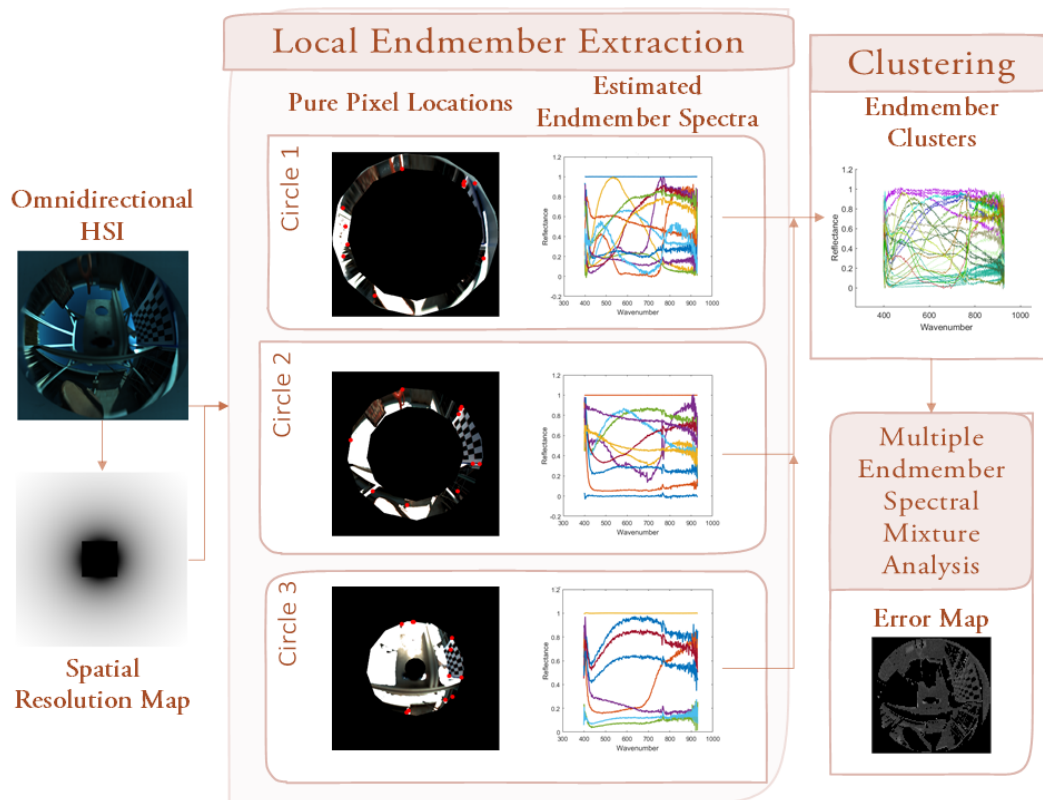
Figure 21: The scheme of the proposed local endmember extraction algorithm.

CHAPTER 5

EXPERIMENTAL RESULTS

In this chapter, the well-known geometrical unmixing approaches and the proposed improvements on geometrical and spatial-contextual unmixing approaches are evaluated. The accuracies of the algorithms are compared on regeneration error.

5.1 Data Definition

In the experiments, seventeen images are evaluated. While the first eleven of them are real world acquisitions, the last five images are synthetically generated catadioptric hyperspectral images. The RGB representations of the experiments are presented in Appendix A.

5.1.1 Synthetic Data

We have simulated a four-wall indoor scene. Each wall is composed of a signature gathered from the Indian Pines dataset [35]. Figure 22a illustrates the perspective view of the cubic room, and Figure 22b is the omnidirectional view. We used the image in the second row to help visualizing the scene easily. The central point coordinate of an omnidirectional image is (0,0,0). The upper and left points from the central point get negative values. The transformation between world point, mirror point and image point is technically and practically presented in the report prepared by Zivkovic and Booij [64]. A world point X is projected to image point $x_{im} = \begin{pmatrix} x_{im} & y_{im} & 1 \end{pmatrix}$:

$$x_{im} = PX = KR[I|C]X \qquad (30)$$

where P is the 3×4 projection matrix that can be decomposed as described above. C is a 3 dimensional vector that represents the position of the camera center. The I above denotes the 3×3 identity matrix. The matrix R is a 3×3 rotation matrix that describes the rotation of the camera with respect to the world frame. The matrix K is the camera calibration matrix:

$$K = \begin{pmatrix} f_x & s & x_0 \\ 0 & f_y & y_0 \\ 0 & 0 & 1 \end{pmatrix} \qquad (31)$$
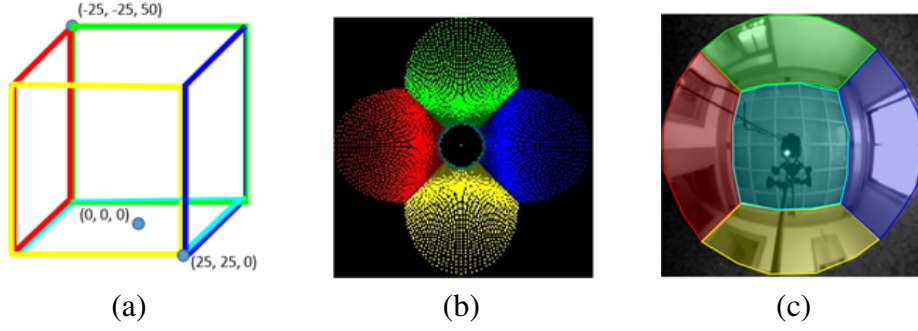
41

Figure 22: (a) The perspective view of the room and the corresponding coordinates. (b) Omnidirectional view of the room. (c) An example illustration for omnidirectional image of a four-wall indoor scene [6].

where f_x and f_y are the scale factors in x and y directions, s is skew and (x_0, y_0) are the image coordinates of the projection of the camera optical center.

A 3D world point X is first projected to the point X_m on the mirror surface:

$$X_m = (x \quad y \quad z \quad 1/\lambda(X))^T, \tag{32}$$

where

$$\lambda(X) = \frac{b^2(-ez - a\sqrt{x^2 + y^2 + z^2})}{b^2 + z^2 - a^2(x^2 + y^2)} \tag{33}$$

The point X_m on the mirror is then projected to the image using the standard perspective camera equations $x_{im} = PX = KR[I|C]X_m$.

The walls have a pattern of strips with 2 pixel width where the consecutive strips have different spectral characteristics. Totally 11 different spectra are used in a simulated image. The spectra are gathered from Indian Pines hyperspectral dataset. The synthetic data is categorized into four parts:

- No noise, pure spectral signature (Experiment #12)

- Noisy, pure spectral signature (Experiments #13 and #14)

- Noisy, two consecutive strips' spectral signatures are mixed manually (Experiments #15 and #16)

- No noise, two consecutive strips' spectral signatures are mixed manually (Experiments #17)

The RGB representations of the categories are demonstrated in Figure 23 (a,b,c). Figure 23d shows the mixing map that demonstrates the mixing ratios of each pixel. The highly mixed pixels get higher values in the map. The map is generated for display purposes. The ratio is computed by multiplying the abundances of a pixel as
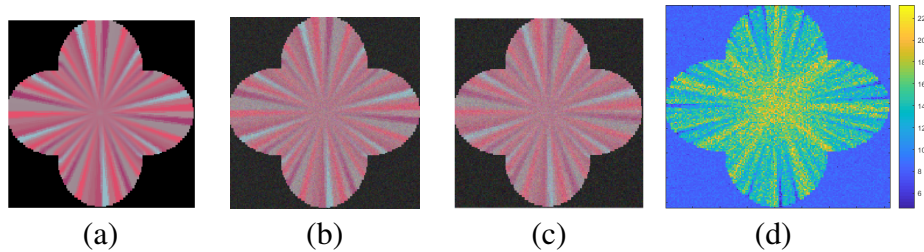
42

Figure 23: Synthetic omnidirectional hyperspectral data (a) No noise, pure spectra. (b) Noisy, pure spectra. (c) Noisy, manually mixed. (d) Mixing map where high intensity indicates higher mixing ratio.

shown in the following formula:

$$\text{mixing map} = \prod_{i=1}^{p}(\mathbf{c}_i + 1) \tag{34}$$

where p is the total number of endmembers, c_i are the mixing abundances. We add one to the abundance values in order to avoid the case which abundance of an endmember is zero. The sum of the abundances for a pixel is as in equation below:

$$\sum_{i=1}^{p} \mathbf{c}_i = 1 \tag{35}$$

5.1.2 Real World Acquisitions

The proposed method is tested on scenes that have been acquired by Headwall A-Series Visible + NIR linescan camera with spectral range of 400 nm - 1100 nm and 1.5 nm spectral resolution. Additionally, we used the hyperbolic mirror of NeoVision. We performed outdoor acquisitions in all experiments in our study. We have acquired three datasets which contain totally eleven images. The images in a dataset include same objects in a variety of positions and illumination conditions. All datasets contain building, sky, and forest in some scenes. Additionally, white reflector (teflon) and black reflector are used for reflectance conversion. The sample RGB representations of the datasets and the materials that exist in the scene are given in Table 4.

- **Dataset #1**
  In the first acquisition, several objects made of clay and mosaic are captured in addition to the materials discussed above. Experiments #1 and #2 belong to the Dataset #1.

- **Dataset #2**
  The scene is composed of the materials with distinctive spectral characteristics
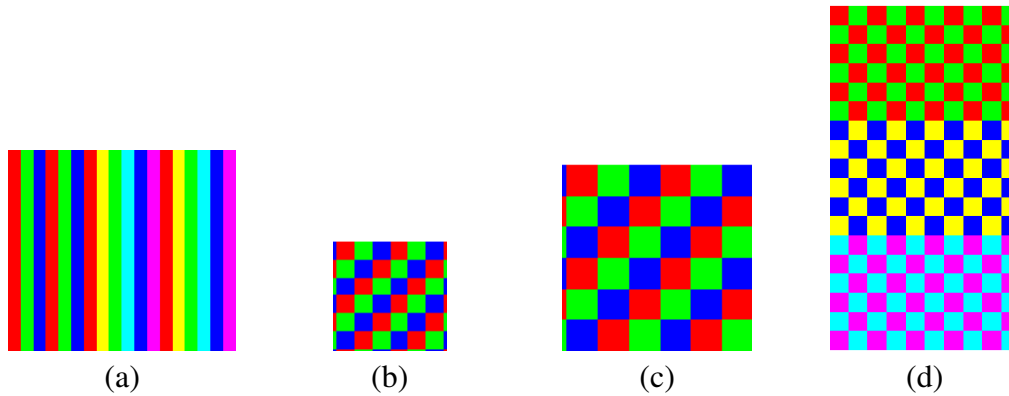
43

Figure 24: Synthetic omnidirectional hyperspectral data (a) No noise, pure spectra. (b) Noisy, pure spectra. (c) Noisy, manually mixed. (d) Mixing map where high intensity indicates higher mixing ratio.

in VNIR region. Bone, vegetation and soil residues can exist together in archaeological remote sensing and food inspection problems. Experiments #3, #4 and #7 to #11 belong to the Dataset #2.

- **Dataset #3**
  The scene contains printed papers with six different colors on different geometrical shapes. The shapes are painted by using red, green, blue, magenta, cyan and yellow colors. The first print (Figure 24) covers 6 color stripes which lie from outer regions to the center of the image. Two of the prints are painted by red, green and blue, and the squares' size are $1cm^2$ and $2cm^2$ (Figure 24b and c). The last paper (Figure 24d) is designed contrary to the premise of the proposed algorithm. The paper is divided into three parts from outer to the center of the image. Each part contains different 2 colored squares. The colors which exist in the inner part, do not exist in the outer part. Experiments #5 and #6 belong to the Dataset #3.

  The sample RGB representations of the datasets and the materials that exist in the scene are given in Table 4.

5.1.3 Limitations

In principal, imaging is based on measuring the light reflected from the object, the measured value depends on the light that illuminates the scene. The spectral signature taken from the uncalibrated data contains the signature of the light in the scene. The camera requires a stable light source in order to obtain an accurate measurement. Therefore, we need a reliable light source for indoor experiments. Quartz Tungsten Halogen Lamp is a stable light source with a known spectral signature. Figure 32 shows an experiment acquired by using VNIR hyperspectral camera and Quartz Tungsten Halogen Lamp. A ring illumination is used in this study, and it is focused

to illuminate the center of the FOV of the camera. As seen in the figure, the mirror gets a dark view and does not reflect the scene. Because these type of specialized illuminators are only able to illuminate the targeting object rather than the whole environment. As the omnidirectional mirrors capture the 360 degree view of the scene, these illuminators are incapable for the system proposed in this study. For omnidirectional imaging, multiple illuminators must be integrated for the diffuse illumination of the environment to be captured. However, we performed only outdoor acquisitions because of the insufficient illumination equipment.
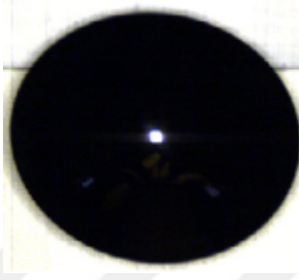

Figure 25: Indoor acquisition example. A dark view of the environment.

5.2 Comparison of Methods

In this section, the well-known geometrical unmixing approaches and the proposed improvements on geometrical and spatial-contextual unmixing approaches are evaluated. The accuracies of the algorithms are compared on regeneration error.

Evaluation Criteria

In this subsection, we compare the effect of the spatial-contextual preprocessing approaches on the performance of the geometrical unmixing algorithms. The methods are compared on the error of regenerated data which is created by using the extracted endmembers. The outputs of the unmixing algorithms are the endmembers($\mathbf{E}$). The size of the matrix $\mathbf{E}$ is $(L \times p)$ where L is the number of spectral bands, and p is the number of endmembers. The abundances of the endmembers are computed by A Fast Non-negativity-Constrained Least Squares Algorithm [56]. $\mathbf{C}$ contains the abundances in each pixel. The size of the abundance matrix ($\mathbf{C}$) is $(p \times N)$ where N is total number of pixels ($rows \times columns$).

$$\mathbf{X} = \mathbf{E}\mathbf{C} + \varepsilon \tag{36}$$

$$RMSE = \sqrt{\frac{\sum_{i=1}^{N}(\mathbf{S}(i,:)^2 - \mathbf{X}(i,:)^2)}{N}} \tag{37}$$

where $\mathbf{S}$ is original hyperspectral data $(L \times N)$, $\mathbf{X}$ is measured hyperspectral data $(L \times N)$, and ε is the noise. The difference between S and X is the error which is used to evaluate the developed algorithms. The difference is measured by the Root

Mean Squared Error (Eq. 37). The error values are increased by 100 times in order to make a more clear evaluation.

5.2.1 Comparison of Unmixing Algorithms and Preprocessing Approaches

In this subsection, the performances of the geometrical unmixing algorithms and the preprocessing approaches are compared. The methods are compared on the error of regenerated data which is created by using the extracted endmembers. The error values are multiplied by 100 for display purposes. In Table 6, the first super-column (containing 3 columns) shows the results of the geometrical unmixing algorithms without any spatial-spectral preprocessing. The following two super-columns contain the results of the spatial-spectral preprocessing approaches (SSPP and Omni-Approach) applied before the regarding geometrical unmixing approaches. The experiments whose results are shared in Table 6, the data id between 1 and 11 are the real world acquisitions, and the rest correspond to the simulated omnidirectional hyperspectral data. The SNR of the data are given in Table 5.

The last row of the Table 6 indicates the overall accumulated error values of the experiments. This overall results provide us to make a comprehensive comparison of the geometrical and spatial-contextual unmixing approaches. The lowest overall error is obtained when N-FINDR algorithm is applied with Omni-Approach. Additionally, Omni-Approach achieves to decrease the overall error of PPI and VCA algorithms. On the other hand, the endmember estimation accuracy of SSPP preprocessing approach highly depends on the estimated number of endmembers. In this case, SSPP remains incapable of decreasing the regeneration error of the geometrical unmixing algorithms.

5.2.2 Evaluation of the Proposed Improvement on Geometrical Approaches

In this subsection, we aim to observe the effect of the proposed improvement explained in Section 4.3 on the existing geometrical unmixing algorithms. Table 7 and Table 8 represent the case which satisfies the situation that the proposed improvement is based on. The first column in the table shows the RGB representations of the scenes. The upper row contains the error maps created by VCA and OmniVCA algorithms. Bright tones indicate higher error, dark tones indicate lower error. The second row shows the estimated pure pixel locations on the RGB images of the data. The last row indicates the regeneration errors of the N-FINDR, PPI, and VCA algorithms with and without omnidirectional approach.

5.2.3 Evaluation of the Proposed Local Endmember Extraction Approach

In this subsection, we evaluate the endmember estimation performance of the algorithm proposed in Section 4.5. Figure 27 demonstrates the comparison of the number
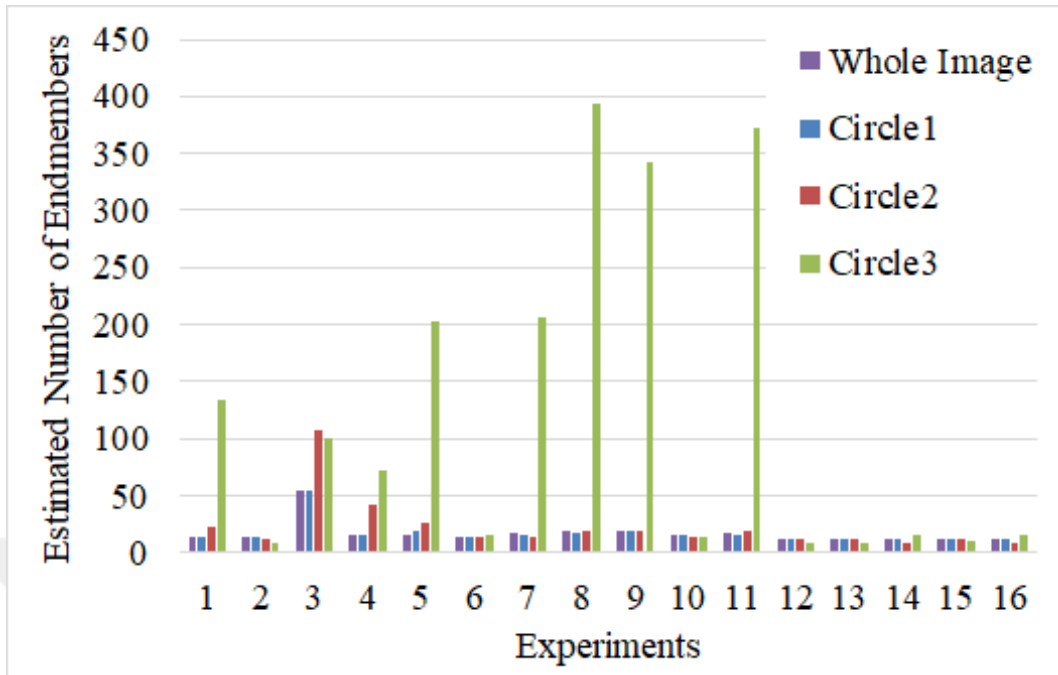
Figure 26: Over-estimated number of endmembers.

of endmembers estimated from individual circles vs. whole image. Circle 1 is the outer, and the circle 3 is the inner one. In the experiments between #12 and #17, 11 different spectral signatures are used. The number of endmembers are estimated highly correlated with the groundtruth in the Exp. #12, #13 and #17. In the Exp. #14, #15, and #16, the noise is increased, and the data is manually mixed. Consequently, estimation accuracy is decreased in these experiments. In most of the experiments, the estimated number of endmembers are similar to each other between circles. However, in Exp. #3, #4, and #5, the estimated number of endmembers are explicitly increased in inner circles.

The extracted endmember locations are demonstrated in Figure 28. As it can be analyzed in the RGB representations, there is no significant material diversity difference between inner and outer circles. The reliability of Hysime is highly dependent on SNR estimation accuracy. In the provided Matlab code by the authors, the signal to noise ratio (SNR) is assigned 50 as default. However, it fails in some cases and the algorithm grossly over-estimates the number of endmembers as in Figure 26. The high number of estimated endmembers provides regenerating the data with lower error. In other respects, the difference between the numbers of endmembers of circles is not reasonable. Therefore, we modified the implementation of the SNR prediction as:

$$\text{SNR} \equiv 10\log_{10}\frac{\mathbf{x}^2}{\sigma^2} \equiv 10\log_{10}\frac{\mathbb{E}[\mathbf{s}^T\mathbf{s}]}{\mathbb{E}[\mathbf{n}^T\mathbf{n}]} \tag{38}$$

where s and n are vectors standing for signal and additive noise, respectively.
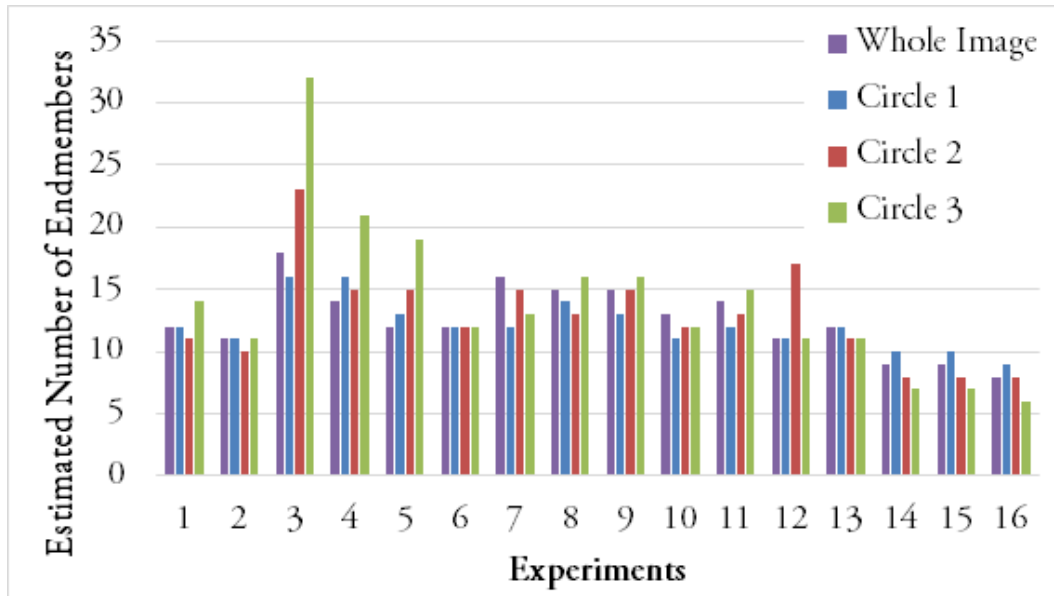
Figure 27: Estimated number of endmembers on each circular division.

As a reminder, the errors are measured per pixel. In other words, the total error of the data is normalized by the total number of pixels. Therefore, the error is independent of the circle size. The proposed improvements are compared in Table 9. The first column shows the regeneration error without using a spatial information. The following column contains the results which obtained by using only the OmniVCA approach. Figure 30 and Table 9 show that the simulated images produce lower errors due to their comparatively higher SNR values. The overall error is reduced by 3% with OmniVCA approach. The last column presents the results of the algorithm where the OmniVCA and local EEA algorithms are used together. The significant contribution is obtained in the local EEA and multiple endmember selection approach. The overall error in this column decreases 45% compared to the VCA approach with no spatial information.

The experimental results shared in Table 9 correspond to the results of the evaluation of 3 circles. The performance of the local EEA approach is evaluated for 2, 3, 9, and 18 circular divisions and sub-regions. Therefore, we measure the relation between the subset size and performance of the algorithm. The schemes of the divisions are demonstrated in Figure 29. The chart in Figure 30 compares the subset sizes on reconstruction error. The study [59] proposes to set the subset size as 10% of the image size. However, in this study, we obtain lowest error by using 3 circles, in other words, 33% of the image size. In other respects, the image is partitioned into tori with equal minor radii. In this case, the inner circle has least number of pixels, and the outer circle has most number of pixels. In most of the scenes, the inner circle captures the highly saturated area e.g., sky and aluminum camera holder. HySime mostly fails in estimation of number of endmembers in these scenes. Therefore, we continue the studies by keeping equal the number of pixels rather than minor radii. As the region size decreases, the algorithm for estimation of number of endmembers
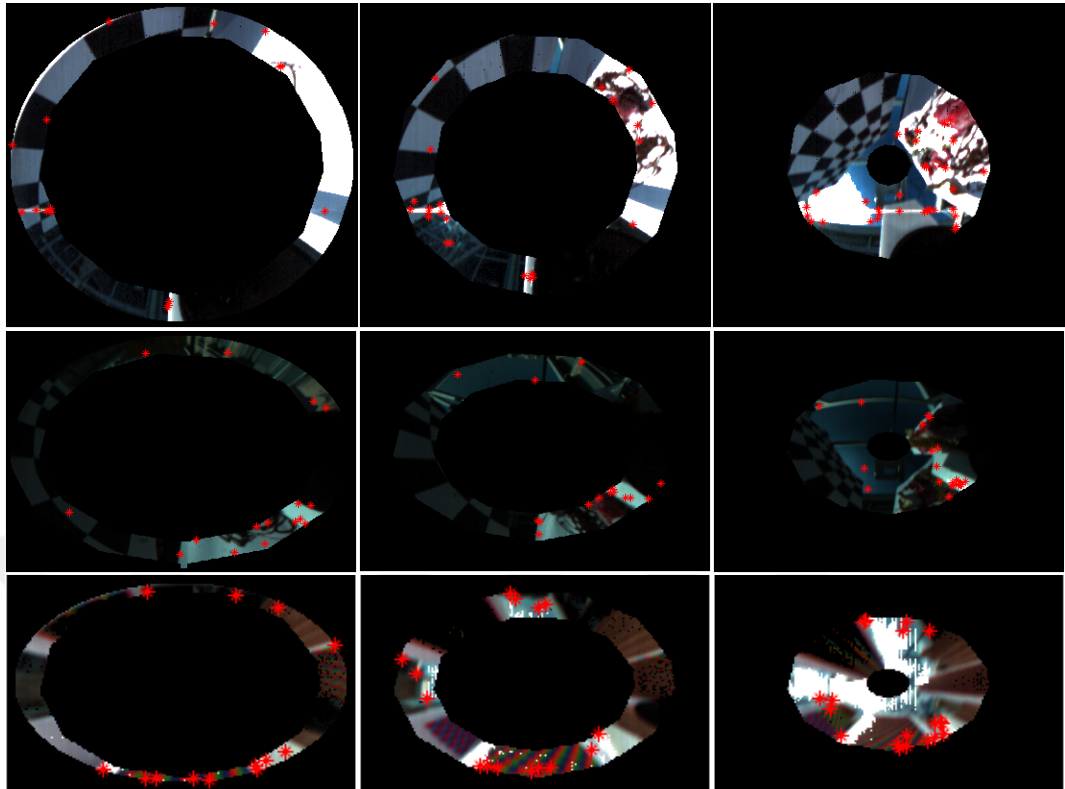
Figure 28: Extracted endmembers on each circular division (from up to down, respectively, Exp. #3, Exp. #4, Exp. #5).
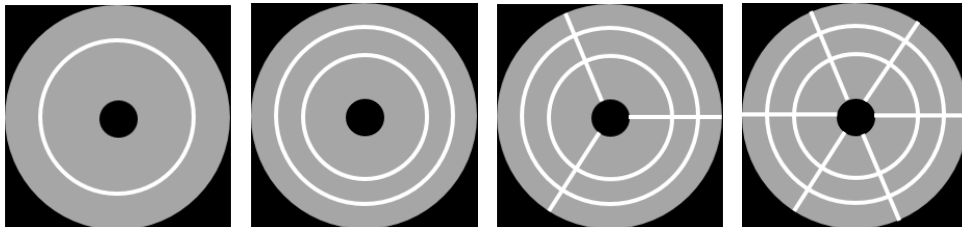

Figure 29: Circular Divisions.

(HySime) underperforms. The output of the HySime algorithm directly effects the extracted endmember spectra and the regeneration performance.

5.3 Discussion

While N-FINDR searches all pixels for pure pixel detection, VCA has only computational cost of iteration as number of endmembers. Therefore VCA has considerably lower computational cost than N-FINDR. As it is indicated in the performance evaluation of study presented in [43], VCA performs better than or comparable to
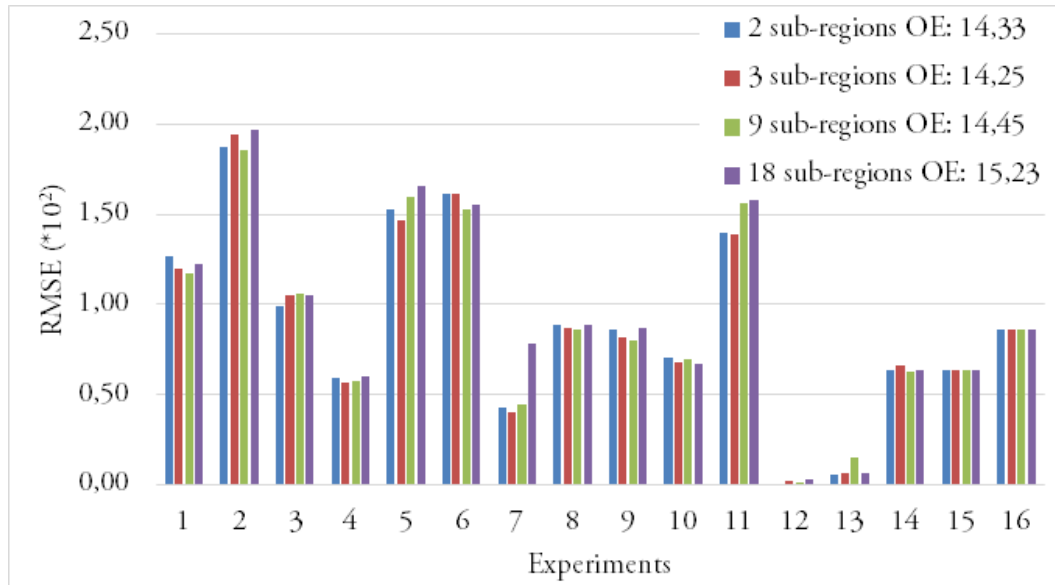
Figure 30: Reconstruction errors for each circular division.

N-FINDR. Additionally, the presented experimental studies show that VCA produces lower regeneration error than PPI and NFINDR.

VCA, PPI, and N-FINDR aim to find the minimum volume containing the data, and the extreme points on the simplex correspond to the endmembers. However, it limits the performance of the algorithms for the mixed pixels with a higher brightness than the unmixed pixels [42].The saturated pixels are always constitute the vertices of the simplex.

The proposed improvement on geometrical unmixing approaches (Omni-Approach) specific to the omnidirectional hyperspectral imaging system, succeeded in increasing the performance of the state-of-the-art VCA method on most of the experiments. However, scenes which contain different materials on the inner and the outer parts of the mirror limit the potential of the method.

The proposed local EEA method is also developed according to the structure of the omnidirectional hyperspectral imaging system. Both of the improvements proposed in this study are applied concurrently on hyperspectral data. We conclude that the spectral analysis of omnidirectional data achieves higher performance on spatially divided parts rather than implementing on whole image. The endmembers and their abundances are properly estimated by using circular divisions.
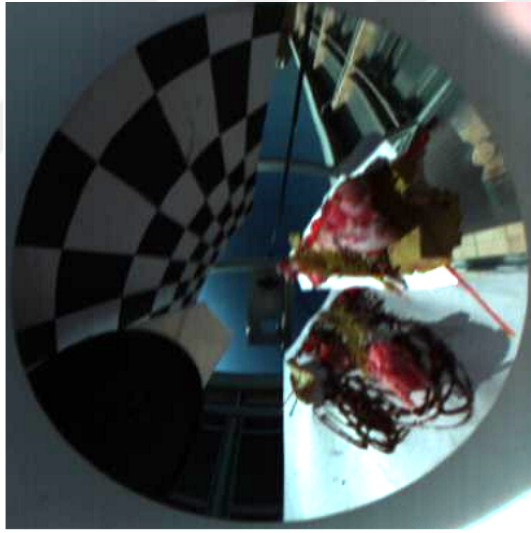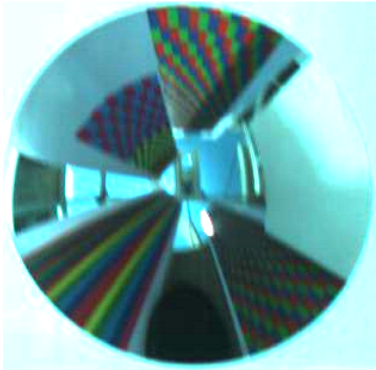
Table 4: Details of the Real World Acquisitions

	RGB images	Materials existing in the scene
Dataset #1		- B&W checkerboard - Teflon (white reflector) - Several objects (clay) - Mosaic - Building - Camera holder aluminium - Sky - Forest
Dataset #2		- B&W checkerboard - Teflon (white reflector) - Black reflector - Bone - Leaf - Soil - Building - Camera holder aluminium - Sky
Dataset #3		6 color prints - Teflon (white reflector) - Building - Camera holder aluminium - Sky

51

Table 5: SNR Values and The Datasets Belonging to The Experiments (Low SNR Value Indicates High Noise, SIM: Simulated Data)

Exp.#	Dataset#	SNR
1	1	31
2	1	30
3	2	34
4	2	26
5	3	29
6	3	26
7	2	28
8	2	32
9	2	32
10	2	26
11	2	34
12	sim.	*no noise*
13	sim.	50
14	sim.	30
15	sim.	50
16	sim.	30
17	sim.	*no noise*

Table 6: Regeneration Error Based Comparison of Geometrical Unmixing Algorithms with and without Preprocessing Approaches (OE: Overall Error)

Exp.#	Geometrical Approaches			Spatial-Spectral Approaches					
	No preprocessing			SSPP			Omni-Approach		
	NFINDR	PPI	VCA	NFINDR	PPI	VCA	NFINDR	PPI	VCA
1	1.97	3.85	1.81	1.94	4.40	2.40	1.72	5.74	1.86
2	2.26	7.27	2.92	2.43	7.01	4.94	2.12	8.12	2.92
3	1.35	4.76	2.49	1.46	2.67	2.00	2.13	2.39	1.75
4	1.05	2.57	1.04	1.05	2.16	0.94	1.05	2.87	0.97
5	2.68	9.43	2.71	5.19	19.35	3.14	2.51	12.38	2.78
6	2.47	9.33	2.42	11.90	10.23	2.51	2.56	9.43	2.63
7	3.85	5.21	1.62	5.13	4.46	1.91	1.90	5.21	1.76
8	1.52	4.19	1.46	1.49	4.15	1.43	1.50	3.92	1.61
9	1.71	3.54	1.60	1.60	4.00	1.46	1.43	3.76	1.55
10	1.36	3.25	1.57	1.37	2.35	1.33	1.42	2.41	1.57
11	1.50	6.84	2.69	1.57	6.06	2.38	1.39	6.37	2.69
12	0.03	24.07	0.00	0.43	23.36	0.43	0.03	11.65	0.00
13	0.09	23.30	1.77	0.36	29.03	1.58	0.08	23.31	1.24
14	0.94	12.44	0.64	1.05	30.13	0.83	0.80	11.55	0.64
15	0.94	12.54	0.65	1.03	30.20	0.92	0.80	25.94	0.65
16	1.30	24.69	0.89	1.29	30.90	1.10	1.09	13.81	0.88
17	0.03	12.21	0	0.12	28.97	0.10	0.03	11.66	0
OE	25.05	169.49	26.28	39.40	239.40	29.40	22.54	160.51	25.51

53

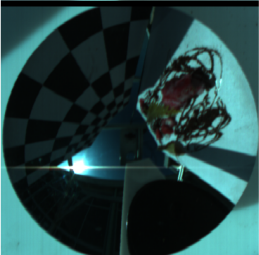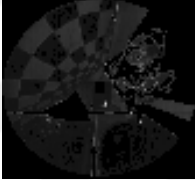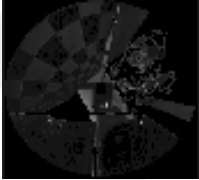Table 7: The Evaluation of the Proposed Geometrical Unmixing Improvement on Exp. #3

RGB Representation	Error Map of VCA	Error Map of OmniVCA
	Pure Pixel Locations of VCA	Pure Pixel Locations of OmniVCA
	Original Algorithms			Omni Approach		
	NFINDR	PPI	VCA	NFINDR	PPI	VCA
	1.35	4.76	2.49	2.13	2.39	1.75

Table 8: The Evaluation of the Proposed Geometrical Unmixing Improvement on Exp. #4
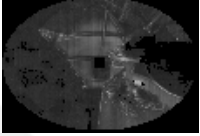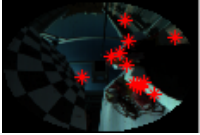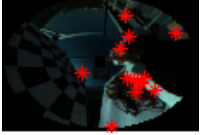
RGB Representation	Error Map of VCA		Error Map of OmniVCA		
	Pure Pixel Locations of VCA		**Pure Pixel Locations of OmniVCA**		
	Original Algorithms			**Omni Approach**	
	NFINDR	PPI	VCA	NFINDR	PPI	VCA
	1.50	2.25	1.44	1.46	2.19	1.30

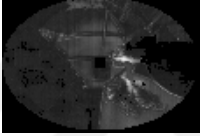Table 9: Regeneration Error Based Performance Evaluation of the Proposed Improvements (OE: Overall Error)

Exp.#	VCA no preprocessing	VCA Omni-Approach	VCA Omni-Approach & Local EEA
1	1.81	1.86	1.20
2	2.92	2.92	1.94
3	2.49	1.75	1.05
4	1.04	0.97	0.57
5	2.71	2.78	1.47
6	2.42	2.63	1.62
7	1.62	1.76	0.41
8	1.46	1.61	0.87
9	1.60	1.55	0.82
10	1.57	1.57	0.68
11	2.69	2.69	1.39
12	0.00	0.00	0.02
13	1.77	1.24	0.07
14	0.64	0.64	0.66
15	0.65	0.65	0.64
16	0.89	0.88	0.86
17	0	0	0.01
OE	26.28	25.51	14.26

CHAPTER 6

CONLUSION

The hyperspectral cameras used in remote sensing applications often need large field of view (FOV). Recent applications capture large FOV hyperspectral data by using airborne, satellite and UAV systems. In this study, we aimed to increase the FOV of traditional hyperspectral imaging systems. The limitations of existing systems, weather conditions, flight permissions, no fly zones, costly aircraft hire, and carrying capacity of UAVs, are alleviated in low cost and easy-to-use manner. We proposed using line scan cameras on catadioptric systems. To our knowledge, this is the first time that a single hyperspectral camera and a single catadioptric mirror is used together to capture an omnidirectional hyperspectral image.

We analyzed the proposed system in the context of spectral unmixing which is one of the most challenging problems of hyperspectral imaging. We identified the critical issues on spectral unmixing that must be taken into consideration specifically for the proposed system, and we investigated these points technically and practically.

Because the proposed system performs the chemical analysis of the object to be captured, all factors between imaging device and the object must be examined carefully. Therefore, we performed measurements and literature search on the spectral effect of the illumination and the material of the mirror. The experimental results show that the spectral characteristic of stainless steel does not constitute an impediment to the usage of mirrors on omnidirectional hyperspectral image analysis.

The spatial-contextual approaches on conventional unmixing algorithms need to be re-implemented according to the mirror formation. The spatial distances between pixels are not uniform in catadioptric imaging. The distance parameter of the spatial-spectral unmixing approach was computed due to the structure of the mirror.

Another approach on spectral analysis covers the geometrical unmixing algorithms. As the region closer to the center of the mirror has lower spatial resolution, we introduced a weighting scheme to favor pure pixels in the outer part of the mirror. The weighing approach OmniVCA reduced the overall regeneration error 3% compared to the original VCA approach. Lastly, the local unmixing approach on hyperspectral image analysis was adapted specifically to the proposed imaging system, and we developed a new spatially local unmixing approach. The novel approach significantly (45%) increases the performance of the conventional geometrical and spatial-contextual unmixing algorithms on estimating the endmembers and their abundances.

57

As future work, we suggest an intelligent endmember selection process in the multiple endmember spectral mixture analysis e.g., incorporating spectral similarity of the spatially neighboring pixels, developing an effective clustering method by using the variances. Additionally, regional division step of local unmixing approach can be performed adaptively based on uniform spectral properties of regions instead of equal sized ones. On the other hand, the relation between the scene content and the position of the divider line can be investigated for the vertical divisions. Furthermore, nonlinear unmixing analysis can be investigated for catadioptric image formation.

The proposed system covers many application areas belonging to the omnidirectional and hyperspectral imaging. The study may produce a practical solution for the problems which requires wide field of view including gas emission detection, road traffic monitoring, biomedical imaging and surveillance.

REFERENCES

[1] F. E. Nicodemus, J. C. Richmon, J. J, I. W. Ginsberg, and T. Limperis, *Geometrical considerations and nomenclature for reflectance*, vol. 160. US Department of Commerce, National Bureau of Standards, 1977.

[2] M. Benlattar, E. M. Oualim, M. Mazroui, A. Mouhsen, M. Harmouchi, and others, "Stainless-steel thin film as passive radiative cooling materials," *Optics and Photonics Journal*, vol. 6, no. 08, p. 193, 2016.

[3] H. Rooms, D. Hermes, S. Harkema, C. Tanase, T. van Mol, P. W. M. Blom, and J. Wilson, "Optimization of the efficacy and angle dependence of emission of top-emissive organic light-emitting diodes on metal foils," *Journal of Photonics for Energy*, vol. 1, no. 1, p. 11024, 2011.

[4] L. Marot, G. De Temmerman, P. Oelhafen, G. Covarel, and A. Litnovsky, "Rhodium coated mirrors deposited by magnetron sputtering for fusion applications," *Review of Scientific Instruments*, vol. 78, no. 10, p. 103507, 2007.

[5] T. L. Bergman, F. P. Incropera, D. P. DeWitt, and A. S. Lavine, *Fundamentals of heat and mass transfer*. John Wiley & Sons, 2011.

[6] J. Zeng, X. Su, and G. Jin, "Incorporating lens distortion into the design of undistorted catadioptric omnidirectional cameras," *Applied Optics*, vol. 45, p. 7778, 10 2006.

[7] C. Thomas, T. Ranchin, L. Wald, and J. Chanussot, "Synthesis of multispectral images to high spatial resolution: A critical review of fusion methods based on remote sensing physics," *IEEE Transactions on Geoscience and Remote Sensing*, vol. 46, no. 5, pp. 1301–1312, 2008.

[8] P. Latorre-Carmona, J. Martinez Sotoca, F. Pla, J. Bioucas-Dias, and C. Julia Ferre, "Effect of denoising in band selection for regression tasks in hyperspectral datasets," *IEEE Journal of Selected Topics in Applied Earth Observations and Remote Sensing*, vol. 6, no. 2, pp. 473–481, 2013.

[9] L. M. Bruce, C. H. Koger, and J. Li, "Dimensionality reduction of hyperspectral data using discrete wavelet transform feature extraction," *Geoscience and Remote Sensing, IEEE Transactions on*, vol. 40, no. 10, pp. 2331–2338, 2002.

[10] J. Wang and C.-I. Chang, "Independent component analysis-based dimensionality reduction with applications in hyperspectral image analysis," *Geoscience and Remote Sensing, IEEE Transactions on*, vol. 44, no. 6, pp. 1586–1600, 2006.

[11] K. Jia, B. Wu, Y. Tian, Q. Li, and X. Du, "Spectral discrimination of opium poppy using field spectrometry," *Geoscience and Remote Sensing, IEEE Transactions on*, vol. 49, no. 9, pp. 3414–3422, 2011.

[12] T. R. Tooke, N. C. Coops, N. R. Goodwin, and J. A. Voogt, "Extracting urban vegetation characteristics using spectral mixture analysis and decision tree classifications," *Remote Sensing of Environment*, vol. 113, no. 2, pp. 398–407, 2009.

[13] J.-J. Wang, Y. Zhang, and C. Bussink, "Unsupervised multiple endmember spectral mixture analysis-based detection of opium poppy fields from an EO-1 Hyperion image in Helmand, Afghanistan," *Science of The Total Environment*, vol. 476, pp. 1–6, 2014.

[14] J. Gluckman and S. K. Nayar, "Catadioptric Stereo Using Planar Mirrors," Tech. Rep. 1, 2001.

[15] Y. Bastanlar, *Structure-from-motion for systems with perspective and omnidirectional cameras*. PhD thesis, Ph. D. Thesis, Middle East Technical University, 2009.

[16] Aeromeccanica, "Fly360." \url{http://www.aeromeccanica.it/}.

[17] Technest Holdings, "REAL-TIME OMNI-DIRECTIONAL HYPERSPECTRAL IMAGER | SBIR.gov," 2006.

[18] K. Hirai, N. Osawa, M. Hori, T. Horiuchi, S. Tominaga, K. Hirai, N. Osawa, M. Hori, T. Horiuchi, and S. Tominaga, "High-dynamic-range spectral imaging system for omnidirectional scene capture," *Journal of Imaging*, vol. 4, p. 53, 3 2018.

[19] A. C. Karaca, A. Erturk, M. K. Gullu, and S. Erturk, "Ground-based panoramic stereo hyperspectral imaging system with multiband stereo matching," *IEEE Journal of Selected Topics in Applied Earth Observations and Remote Sensing*, vol. 9, pp. 3926–3940, 9 2016.

[20] S. Tominaga, T. Fukuda, and A. Kimachi, "A high-resolution imaging system for omnidirectional illuminant estimation," *Journal of Imaging Science and Technology*, vol. 52, no. 4, p. 040907, 2008.

[21] K. Danilidis, E. Angelopoulou, and V. Kumar, "Multispectral omnidirectional optical sensor and methods therefor," 1 2006.

[22] Y. Xue, K. Zhu, Q. Fu, X. Chen, and J. Yu, "Catadioptric HyperSpectral Light Field Imaging," in *2017 IEEE International Conference on Computer Vision (ICCV)*, pp. 985–993, IEEE, 10 2017.

[23] J. C. Bazin, C. Demonceaux, P. Vasseur, and I.-S. Kweon, "Motion estimation by decoupling rotation and translation in catadioptric vision," *Computer Vision and Image Understanding*, vol. 114, no. 2, pp. 254–273, 2010.

[24] I. Cinaroglu and Y. Bastanlar, "A direct approach for object detection with catadioptric omnidirectional cameras," *Signal, Image and Video Processing*, vol. 10, pp. 413–420, 2 2016.

[25] M. Lourenco, J. P. Barreto, and F. Vasconcelos, "sRD-SIFT: Keypoint detection and matching in images with radial distortion," *IEEE Transactions on Robotics*, vol. 28, pp. 752–760, 6 2012.

[26] N. D. Ozisik, G. Lopez-Nicolas, and J. J. Guerrero, "Scene structure recovery from a single omnidirectional image," in *2011 IEEE International Conference on Computer Vision Workshops (ICCV Workshops)*, pp. 359–366, IEEE, 2011.

[27] A. Iraqui, Y. Dupuis, R. Boutteau, J.-Y. Ertaud, and X. Savatier, "Fusion of omnidirectional and PTZ cameras for face detection and tracking," in *2010 International Conference on Emerging Security Technologies*, pp. 18–23, IEEE, 9 2010.

[28] S. Kang, A. Roh, B. Nam, and H. Hong, "People detection method using graphics processing units for a mobile robot with an omnidirectional camera," *Optical Engineering*, vol. 50, p. 127204, 12 2011.

[29] T. Kawanishi, K. Yamazawa, H. Iwasa, H. Takemura, and N. Yokoya, "Generation of high-resolution stereo panoramic images by omnidirectional imaging sensor using hexagonal pyramidal mirrors," in *Pattern Recognition, 1998. Proceedings. Fourteenth International Conference on*, vol. 1, pp. 485–489, IEEE, 1998.

[30] K. Yamazawa, Y. Yagi, and M. Yachida, "Obstacle detection with omnidirectional image sensor hyperomni vision," in *Robotics and Automation, 1995. Proceedings., 1995 IEEE International Conference on*, vol. 1, pp. 1062–1067, IEEE, 1995.

[31] Y. Bastanlar, "Parameter extraction and image enhancement for catadioptric omnidirectional cameras," no. April, 2005.

[32] S. Baker and S. K. Nayar, "A theory of catadioptric image formation," in *Computer Vision, 1998. Sixth International Conference on*, pp. 35–42, IEEE, 1998.

[33] Y. Onoe, K. Yamazawa, H. Takemura, and N. Yokoya, "Telepresence by real-time view-dependent image generation from omnidirectional video streams," *Computer Vision and Image Understanding*, vol. 71, pp. 154–165, 8 1998.

[34] M. Taghizadeh, A. A. Gowen, and C. P. O'Donnell, "Comparison of hyperspectral imaging with conventional RGB imaging for quality evaluation of Agaricus bisporus mushrooms," *Biosystems Engineering*, vol. 108, pp. 191–194, 2 2011.

[35] M. F. Baumgardner, L. L. Biehl, and D. A. Landgrebe, "220 Band AVIRIS hyperspectral image data set: June 12, 1992 Indian Pine Test Site 3," 2015.

[36] R. B. Singer and T. B. McCord, "Mars-large scale mixing of bright and dark surface materials and implications for analysis of spectral reflectance," in *Lunar and Planetary Science Conference Proceedings*, vol. 10, pp. 1835–1848, 1979.

[37] N. Dobigeon, Y. Altmann, N. Brun, and S. Moussaoui, "Linear and Nonlinear Unmixing in Hyperspectral Imaging," *Data Handling in Science and Technology*, vol. 30, pp. 185–224, 1 2016.

[38] J. M. Bioucas-Dias, A. Plaza, N. Dobigeon, M. Parente, Q. Du, P. Gader, and J. Chanussot, "Hyperspectral unmixing overview: Geometrical, statistical, and sparse regression-based approaches," *IEEE Journal of Selected Topics in Applied Earth Observations and Remote Sensing*, vol. 5, pp. 354–379, 4 2012.

[39] X. Zhang, Y. Sun, J. Zhang, P. Wu, and L. Jiao, "Hyperspectral unmixing via deep convolutional neural networks," *IEEE Geoscience and Remote Sensing Letters*, vol. 15, pp. 1755–1759, 11 2018.

[40] J. M. Bioucas-Dias and J. M. P. Nascimento, "Hyperspectral subspace identification," *IEEE Transactions on Geoscience and Remote Sensing*, vol. 46, no. 8, pp. 2435–2445, 2008.

[41] J. W. Boardman, "Automating spectral unmixing of AVIRIS data using convex geometry concepts," 1993.

[42] M. E. Winter, "N-FINDR: An algorithm for fast autonomous spectral endmember determination in hyperspectral data," in *SPIE's International Symposium on Optical Science, Engineering, and Instrumentation*, pp. 266–275, International Society for Optics and Photonics, 1999.

[43] J. M. P. Nascimento and J. M. B. Dias, "Vertex component analysis: A fast algorithm to unmix hyperspectral data," *IEEE Transactions on Geoscience and Remote Sensing*, vol. 43, no. 4, pp. 898–910, 2005.

[44] X. Xu, X. Tong, A. Plaza, J. Li, Y. Zhong, H. Xie, and L. Zhang, "A new spectral-spatial sub-pixel mapping model for remotely sensed hyperspectral imagery," *IEEE Transactions on Geoscience and Remote Sensing*, vol. 56, pp. 6763–6778, 11 2018.

[45] Y. Yan, W. Hua, X. Liu, Z. Cui, and D. Diao, "Spatial–spectral preprocessing for spectral unmixing," *International Journal of Remote Sensing*, vol. 40, pp. 1357–1373, 2 2019.

[46] A. Plaza, P. Martinez, R. Pérez, and J. Plaza, "Spatial/spectral endmember extraction by multidimensional morphological operations," *IEEE Transactions on Geoscience and Remote Sensing*, vol. 40, no. 9, pp. 2025–2041, 2002.

[47] M. Zortea and A. Plaza, "Spatial preprocessing for endmember extraction," *IEEE Transactions on Geoscience and Remote Sensing*, vol. 47, no. 8, pp. 2679–2693, 2009.

[48] G. Martin and A. Plaza, "Region-based spatial preprocessing for endmember extraction and spectral unmixing," *IEEE Geoscience and Remote Sensing Letters*, vol. 8, no. 4, pp. 745–749, 2011.

[49] G. Martin and A. Plaza, "Spatial-spectral preprocessing prior to endmember identification and unmixing of remotely sensed hyperspectral data," *IEEE Journal of Selected Topics in Applied Earth Observations and Remote Sensing*, vol. 5, no. 2, pp. 380–395, 2012.

[50] N. Otsu, "A Threshold Selection Method from Gray-Level Histograms," *IEEE Transactions on Systems, Man, and Cybernetics*, vol. 9, pp. 62–66, 1 1979.

[51] J. A. Richards and X. Jia, "Remote sensing digital image analysis: an introduction," 2006.

[52] D. C. Heinz and others, "Fully constrained least squares linear spectral mixture analysis method for material quantification in hyperspectral imagery," *IEEE transactions on geoscience and remote sensing*, vol. 39, no. 3, pp. 529–545, 2001.

[53] D. Heinz, C.-I. Chang, and M. L. G. Althouse, "Fully constrained least-squares based linear unmixing [hyperspectral image classification]," in *Geoscience and Remote Sensing Symposium, 1999. IGARSS'99 Proceedings. IEEE 1999 International*, vol. 2, pp. 1401–1403, IEEE, 1999.

[54] J. J. Settle and N. A. Drake, "Linear mixing and the estimation of ground cover proportions," *International Journal of Remote Sensing*, vol. 14, no. 6, pp. 1159–1177, 1993.

[55] C.-I. Chang and D. C. Heinz, "Constrained subpixel target detection for remotely sensed imagery," *IEEE Transactions on Geoscience and Remote Sensing*, vol. 38, no. 3, pp. 1144–1159, 2000.

[56] R. Bro and S. De Jong, "A fast non-negativity-constrained least squares algorithm," *Journal of Chemometrics*, vol. 11, pp. 393–401, 9 1997.

[57] A. N. Bashkatov, E. A. Genina, V. I. Kochubey, and V. V. Tuchin, "Optical properties of human cranial bone in the spectral range from 800 to 2000 nm," in *Proc. SPIE*, vol. 6163, p. 616310, 2006.

[58] K. A. Schenkman, D. R. Marble, D. H. Burns, and E. O. Feigl, "Myoglobin oxygen dissociation by multiwavelength spectroscopy," *Journal of Applied Physiology*, vol. 82, no. 1, pp. 86–92, 1997.

[59] B. Somers, M. Zortea, A. Plaza, and G. P. Asner, "Automated extraction of image-based endmember bundles for improved spectral unmixing," *IEEE Journal of Selected Topics in Applied Earth Observations and Remote Sensing*, vol. 5, no. 2, pp. 396–408, 2012.

[60] M. A. Goenaga, M. C. Torres-Madronero, M. Velez-Reyes, S. J. Van Bloem, and J. D. Chinea, "Unmixing analysis of a time series of Hyperion images over the Guánica dry forest in Puerto Rico," *IEEE Journal of Selected Topics in Applied Earth Observations and Remote Sensing*, vol. 6, no. 2, pp. 329–338, 2013.

[61] D. A. Roberts, M. Gardner, R. Church, S. Ustin, G. Scheer, and R. O. Green, "Mapping chaparral in the Santa Monica Mountains using multiple endmember spectral mixture models," *Remote sensing of environment*, vol. 65, no. 3, pp. 267–279, 1998.

[62] J. Degerickx, D. Roberts, and B. Somers, "Enhancing the performance of Multiple Endmember Spectral Mixture Analysis (MESMA) for urban land cover mapping using airborne lidar data and band selection," *Remote Sensing of Environment*, vol. 221, pp. 260–273, 2 2019.

[63] S. Lloyd, "Least squares quantization in PCM," *IEEE Transactions on Information Theory*, vol. 28, pp. 129–137, 3 1982.

[64] Z. Zivkovic and O. Booij, "How did we built our hyperbolic mirror omni- directional camera -practical issues and basic geometry How did we built our hyperbolic mirror omnidirectional camera -practical issues and basic geometry Contents,"

<div align="center">

CURRICULUM VITAE

Nur Didem Başkurt

</div>

Research Interest

Hyperspectral Imaging, Omnidirectional Catadioptric Imaging, Computer Vision, Machine Learning

---

Academic Background

Middle East Technical University, Turkey   *2013 - 2019*
Information Systems, Ph.D.
(Qualification Exam: November, 2015)

Universidad de Zaragoza, Spain   *2010 - 2011*
Systems and Computer Engineering, M.Sc.

Universidad de Zaragoza, Spain   *2007 - 2008*
Systems and Computer Engineering, BSc
(Erasmus exchange student)

University of Mersin, Turkey   *2005 - 2009*
Computer Engineering, BSc

Professional Experience

Middle East Technical University, Turkey   *2014 - 2019*
Research and Teaching Assistant

- *Decision Support Systems*

- *Image Processing Algorithms (Matlab)*

- *Introduction to Information Systems*

Atilim University, Turkey   *2013 - 2014*
Teaching Assistant

- *Pattern Recognition*

- *Computer Programming (C)*

- *Database Desing and Management (SQL)*

Publications

- Gur, Yusuf, Fatih Omruuzun, **Didem Özısık Baskurt**, and Yasemin Yardimci Cetin. "Detection of greenhouse gases using infrared hyperspectral imagery." Signal Processing and Communication Application Conference (SIU), 2018 26th. IEEE, 2018.

- **Baskurt, Didem Özısık**, Yusuf Gur, Fatih Omruuzun, and Yasemin Yardimci Cetin. "Gas detection by using transmittance estimation and segmentation approaches." Remote Sensing Technologies and Applications in Urban Environments. Vol. 10008. International Society for Optics and Photonics, 2016.

- Sevim, Hazan Dağlayan, Yasemin Yardımcı Çetin, and **Didem Özışık Başkurt**. "A novel method to detect shadows on multispectral images." Image and Signal Processing for Remote Sensing XXII. Vol. 10004. International Society for Optics and Photonics, 2016.

- **Başkurt, Didem Özişik**, Yusuf Gur, Fatih Omruuzun, and Yasemin Yardimci Cetin "Absorbance estimation and gas emissions detection in hyperspectral imagery." Signal Processing and Communication Application Conference (SIU), 2016 24th. IEEE, 2016.

- Omruuzun, Fatih, **Didem Ozisik Baskurt**, and Yasemin Yardimci Cetin. "DTW based signal alignment for enhancing CO_2 detection in MWIR hyperspectral imagery." Hyperspectral Image and Signal Processing: Evolution in Remote Sensing (WHISPERS), 2015 7th Workshop on. IEEE, 2016.

- Omruuzun, Fatih, **Didem Ozisik Baskurt**, Hazan Daglayan, and Yasemin Yardimci Cetin "Utilizing hyperspectral remote sensing imagery for afforestation planning of partially covered areas." Image and Signal Processing for Remote Sensing XXI. Vol. 9643. International Society for Optics and Photonics, 2015.

- Omruuzun, Fatih, **Didem Ozisik Baskurt**, Hazan Daglayan and Yasemin Yardimci Cetin. "Shadow removal from vnir hyperspectral remote sensing imagery with endmember signature analysis." Next-Generation Spectroscopic Technologies VIII. Vol. 9482. International Society for Optics and Photonics, 2015.

- **Başkurt, Didem Özışık**, Fatih Ömrüuzun, and Yasemin Yardımcı Çetin. "Hyperspectral unmixing based analysis of forested areas." Signal Processing and Communications Applications Conference (SIU), 2015 23th. IEEE, 2015.

- **Özışık, N. D.**, Gonzalo López-Nicolás, and José Jesús Guerrero. "Scene structure recovery from a single omnidirectional image." Computer Vision Workshops (ICCV Workshops), 2011 IEEE International Conference on. IEEE, 2011.

Projects

Hyperspectral Image Analysis of Archaeological Remains, METU   *2015 - 2017*
Researcher

Advanced Imaging Technologies (IGT-TUYGUN), Undersecretariat for Defense and Industries of Turkey   *2014 - 2015*
Researcher
Research Group: Vegetation classification and identification by using hyperspectral images

APPENDIX A
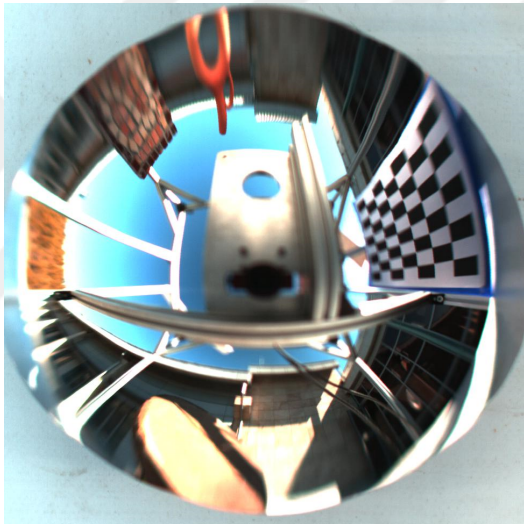
RGB REPRESENTATIONS OF THE EXPERIMENTS

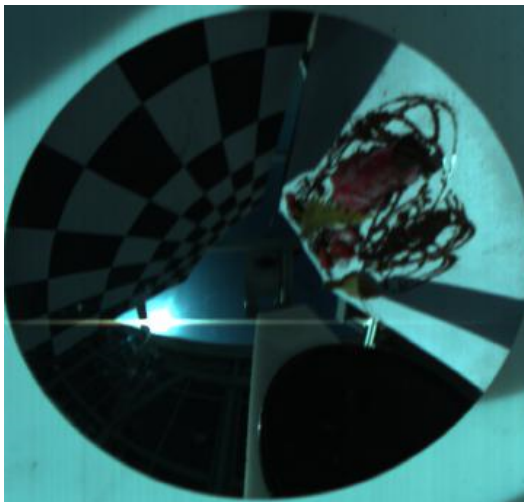Table 10: RGB Representations of the Experiments
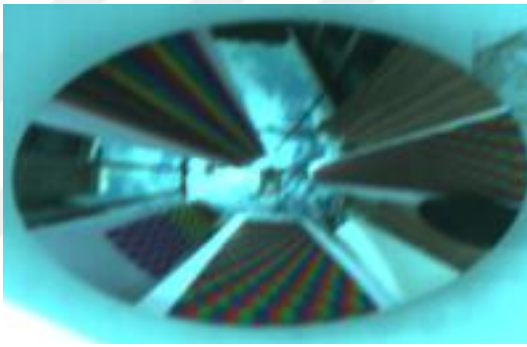
Experiment #1

Experiment #2

Experiment #3

Experiment #4	
Experiment #5	
Experiment #6	
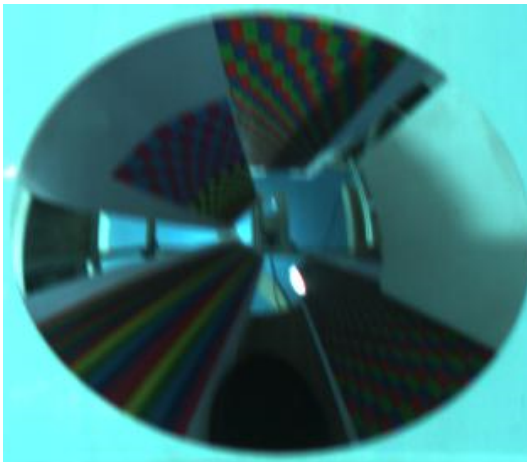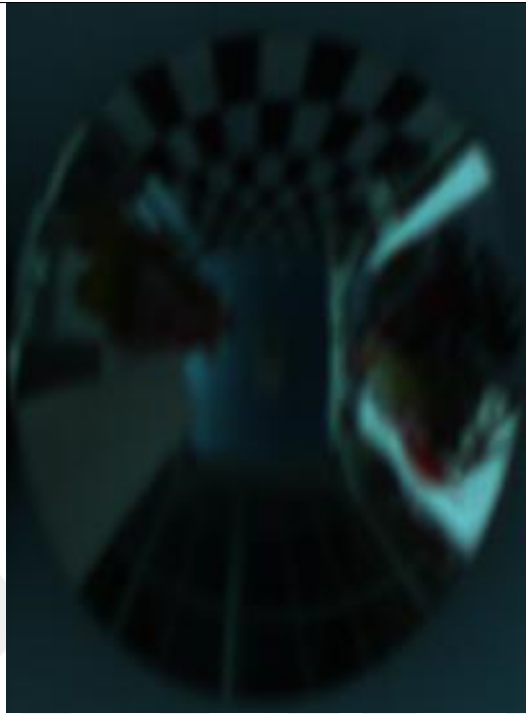
Experiment #7

Experiment #8

Experiment #9
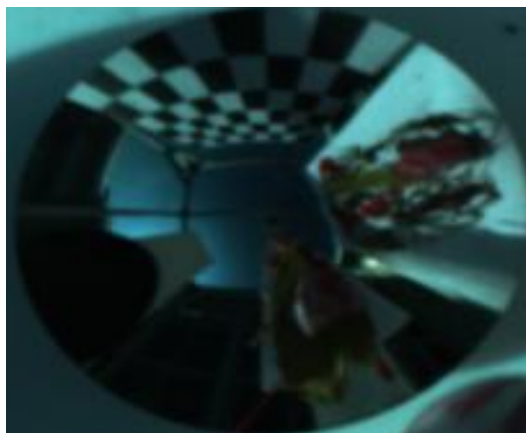
Experiment #10

Experiment #11

Experiment #12
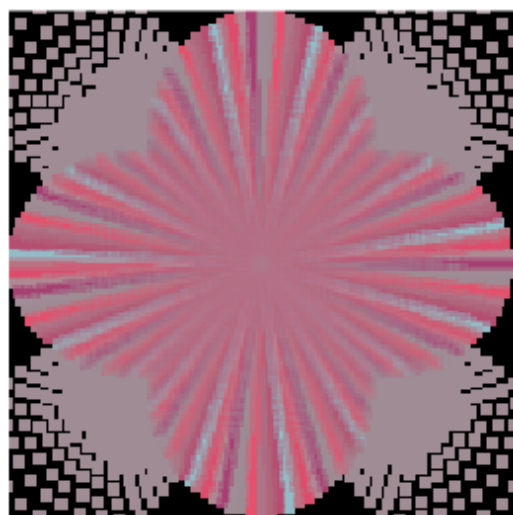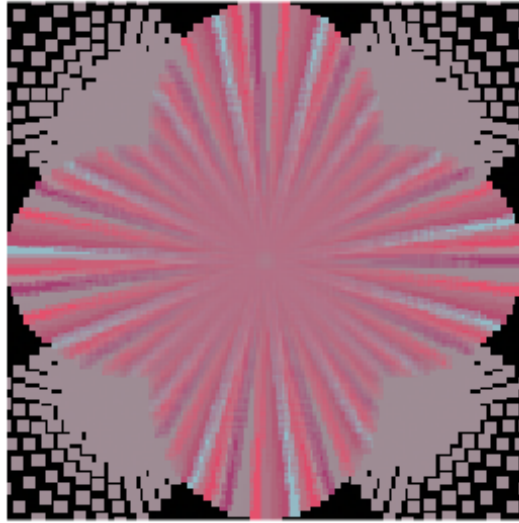
Experiment #13

Experiment #14
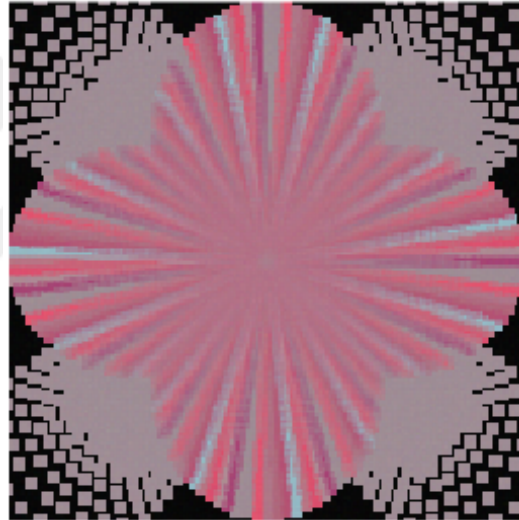
Experiment #15
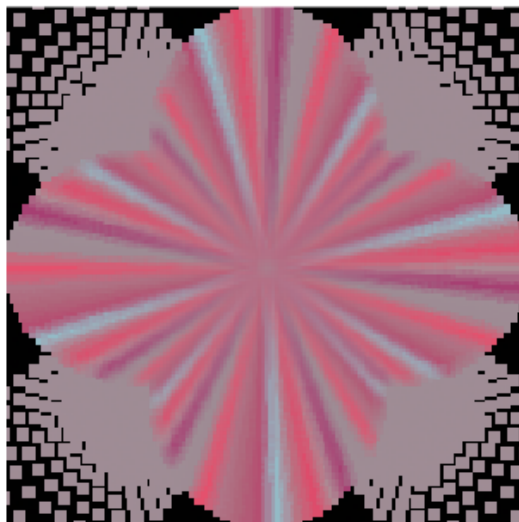
Experiment #16

Experiment #17